The Design and Fabrication of an Electrically Activated Photonic Crystal Microcavity Laser

Alejandro Griñe

B.S.E.E., Electrical Engineering and Computer Science
Minor, Physics
University of New Mexico, 2004

Submitted to the
Department of Electrical Engineering and Computer Science
in partial fulfillment of the requirements for the degree of

Master of Science in Electrical Engineering

at the

MASSACHUSETTS INSTITUTE OF TECHNOLOGY

June 2007

© 2007 Massachusetts Institute of Technology
All rights reserved.

Author........ ....
Alejandro Griñe
Department of Electrical Engineering and Computer Science
February 9, 2007

Certified by.......... ....
Leslie A. Kolodziejski
Professor of Electrical Engineering
Thesis Supervisor

Accepted by....................... ....
Arthur C. Smith
Chair, Department Committee of Graduate Students
Department of Electrical Engineering and Computer Science

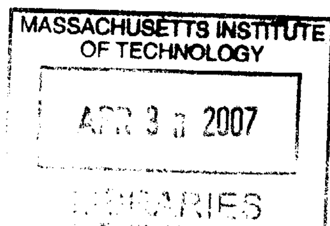
MASSACHUSETTS INSTITUTE OF TECHNOLOGY
2007

ARCHIVES

The Design and Fabrication of an Electrically-Activated Photonic Crystal Microcavity Laser

By
Alejandro Griñe

Submitted to the Department of Electrical Engineering and Computer Science
on February 9, 2007, in partial fulfillment of the
requirements for the degree of
Master of Science in Electrical Engineering

Abstract

Spontaneous emission can be controlled by altering the environment that a medium radiates into; specifically, by reducing the dimensions of a cavity, excited atoms immersed in the cavity are more likely to spontaneously emit photons into the dominant cavity mode than spurious modes. Microcavity lasers exploit this stronger coupling by confining photons to a cavity with outer dimensions approximately the size of an optical wavelength. Owing to the strong coupling to the lasing mode, microcavity lasers are distinguished for their high efficiency, low threshold, high speed, and low noise operation. However, microcavity lasers by nature have low output power. Thus, microcavity lasers are ideal light sources for applications requiring low power such as integrated optics or quantum computation.

This thesis describes the design and fabrication of a microcavity laser utilizing multiple photonic crystal mirrors. The laser is well suited for integrated optics for many reasons. It is electrically activated and emits light in-plane. The laser conserves chip real-estate and couples directly into an output waveguide. The one dimensional photonic crystal mirrors prevent coupling into radiation modes increasing the quality factor (Q) of the cavity. Rate equation analysis is used to show that the laser will have a small threshold current. A new hybrid fabrication scheme is employed that simplifies the device processing. The step and repeat mask design makes it simple to fabricate and to test many devices each with varying dimensions, allowing one to empirically determine the optimal device.

Finally, a new microcavity laser capable of confining light in three dimensions is proposed.

Thesis Supervisor: Leslie A. Kolodziejski
Title: Professor of Electrical Engineering

Acknowledgements

I am truly blessed to have such an outstanding family. Antonette, my wife, and Angelina, my daughter put their entire lives behind them, so I could fulfill a dream. Their sacrifice is something I will never forget. We came to Boston for an adventure, and at times we found ourselves in the middle of a nightmare, but each trial just brought us closer. I now feel that with each others love, no ordeal is insurmountable. I dedicate this thesis to these two amazing, beautiful women. Andrés the next one is for you my friend.

I cannot thank Professor Leslie Kolodziejski enough for first, accepting me into her outstanding group, and second, presenting me with the most intriguing device I could have ever asked for. Upon dealing with Professor Kolodziejski, I can now conclude that she is the equivalent of an optical gain medium, because all who come across her emerge a better person (I apologize for the laser analogy). I am very greatful for both the technical guidance and mentoring that I have received from Leslie during my time as her student.

I also benefited greatly from the technical insights of Dr. Gale Petrich. Throughout my time here he answered all of my many, many questions without ever rolling his eyes (well maybe once!). Everything in this thesis, from mask design to fabrication sequence has a touch of Gale's outstanding ingenuity. I have truly enjoyed our many discussions.

Everyone in the Integrated Photonic Materials and Devices group has been a pleasure to work with. Ryan Williams gave a lot of his time to show me around the clean room and never hesitated to show me any new tricks. Orit Shamir maintained an optimistic attitude even during the days we never left the clean room. She also saved many of my wafers from destruction. My office mate, Reginald Bryant was a model for hard work. It was amazing to witness Reggie's work ethic and genius during our final class-project. I also enjoyed the company of Ta-Ming Shih who always managed to be laid back yet diligent at the same time. This work has spawned from brilliant past members including Solomon Assefa, Alexei Erchak, Eric Mattson, and Ed Lim. I hope I have added a little more pavement to the road.

I would also like to thank my friend, Shahrooz Amin for his sense of humor and never-ending enthusiasm for science. I hope some of it has rubbed off on me. I cannot remember a time I didn't laugh during our regular coffee breaks. Joel Yang was also an outstanding friend. Our regular discussions about family, weekends, and spontaneous emission were always enjoyable.

The atmosphere at MIT is something I will always miss. Even with so much pressure around, everyone was kind and helpful. I thank Jim Daly for selflessly showing me different tools and evaporating metal on all my wafers. Rajeev Ram patiently answered a barrage of my questions after every class.

This work would not have been possible without the support of Sandia National Labs. I owe Armando Sanchez big time for giving my resume to Mitch McCrory, and I owe Mitch McCrory for passing it on to Mike Daily. Finally, I owe Mike Daily for presenting me with this opportunity. I should also thank Dr. Ting, "Willie" Luk for

exposing me to the Bragg Onion Resonator, and Dr. Darwin Serkland for suggesting the use of ITO in my laser design.

My family in Albuquerque has supported me every step of the way. In many ways, this thesis is the result of sacrifices made long ago by my mother and father, Frances and Alfredo Griñe. Waking up every morning, cooking me home made breakfast and then driving me across town to school are just some of the tasks they performed to get me here. My wife's family, Pauline, Rick, and Maggie have contributed in many ways to this thesis. Thank you for not making me pay you back for everything, or else I would be in real trouble.

Finally, I am lucky to have some of the greatest friends in the world whose intelligence and humanitarianism I admire greatly. Ben, Ismail, Ryan, Jon, Mando; bros for life!

Table of Contents

Chapter 1. Introduction 12
1.1. Motivation 12
1.2. Photonic Crystals 13
1.3. Overview 14
Chapter 2. Laser Basics 16
2.1. Background 16
2.2. Semiconductor Lasers 16
2.3. Diode Lasers 18
2.4. The role of spontaneous emission in microcavity lasers 20
2.4.1. Motivation for the Optical Microcavity 21
2.4.2. The quantum-mechanical view of spontaneous emission: Vacuum fields 22
2.5. Other Photonic Crystal Lasers 27
Chapter 3. Design and Simulations 31
3.1. Design Concept 31
3.2. Layered Structure Design 34
3.2.1. Optical Simulations 39
3.3. Rate Equation Calculations 41
3.4. Mask Design 46
3.4.1. Stripe Laser Diagnostic 49
3.4.2. Integrated Diagnostic Detector 51
Chapter 4. Fabrication 52
4.1. Fabrication Sequence 52
4.2. Fabrication Results 55
4.2.1. Steps 1-2: Formation of ohmic contacts on p-type arsenide-based material 55
4.2.2. Steps 3-4: Wet-etching of Arsenide based material 59
4.2.3. Problems with Metal Adhesion 61
4.2.4. Steps 4-5: Formation of ohmic contacts to *n*-type phosphide-based material 66
4.3. Remaining Fabrication Steps: Discussion 66
4.3.1. Steps 7-10: Dry etch of InP and GaAs materials. Patterning of SiO_2 hard mask 67
4.3.2. Steps 11-12: Electron-beam lithography or Focused Ion Beam etching for photonic crystal active region 68
4.3.3. Steps 13-14: Undercut removal of Phosphide-based material 69
4.3.4. Step 15: Etching of SiO_2 to open up contact vias 70
4.3.5. Step 16: Thermal oxidation of AlAs 70
4.4. Fabrication of a generic ridge laser 70
Chapter 5. Conclusion and Future Research 76
5.1. Further Investigations 76
5.1.1. Improvement to the rate equations 76

5.1.2. Testing of the Photonic Crystal Microcavity Laser ... 77
5.1.3. A laser incorporating adiabatic tapers ... 78
5.1.4. A microcavity laser with mirror confinement in three directions ... 78
5.2. Final Conclusions ... 81
Appendix 1: Index of refraction for Al_xGaAs_{1-x} ... 83
Appendix 2: The Phenomenological Rate equations ... 84
Bibliography ... 92

Table of Figures:

FIGURE 1: LIGHT-MATTER INTERACTION PROCESSES ... 17
FIGURE 2: A SIMPLIFIED BAND DIAGRAM OF THE ACTIVE REGION DUE TO PUMPING. SHADED CIRCLES REPRESENT FILLED STATES OR ELECTRONS, WHILE WHITE CIRCLES ARE EMPTY STATES, OR HOLES. CONCEPTS TAKEN FROM [6] ... 18
FIGURE 3 A SIMPLE EDGE EMITTING DIODE LASER WITH MIRRORS ON THE SIDE ... 19
FIGURE 4: EMISSION INTENSITY DISTRIBUTION OF AN X-ORIENTED DIPOLE IN A) FREE SPACE, B) Λ/2 ONE DIMENSIONAL CAVITY WITH FREQUENCY CORRESPONDING TO CUT-OFF, AND C) Λ/2 ONE DIMENSIONAL CAVITY BELOW CUT-OFF. FIGURES AND CONCEPTS FROM [9] ... 20
FIGURE 5: PHOTOLUMINESCENCE SPECTRUM OF FABRY PEROT CAVITIES OF DIFFERENT AXIAL LENGTHS. THE LIGHT IS DETECTED FROM THE CAVITY AXIS. AS THE DIMENSIONS OF THE CAVITY DECREASES, LIGHT IS MORE LIKELY TO BE EMITTED INTO THE LASING MODE. FIGURE IS TAKEN FROM [9]. ... 22
FIGURE 6: TOP VIEW OF A SINGLE DEFECT PHOTONIC CRYSTAL LASER. ... 28
FIGURE 7: ELECTRICALLY ACTIVATED PHOTONIC CRYSTAL LASER DEMONSTRATED IN [26]. ... 29
FIGURE 8: COUPLED CAVITY PHOTONIC CRYSTAL LASER [28]. ... 30
FIGURE 9: SCHEMATIC AND OUTPUT CHARACTERISTICS OF THE LASER DESCRIBED IN [27]. THE SOFT THRESHOLD IS SHOWN IN THE INSET OF THE L-I CURVE. ... 30
FIGURE 10: SCHEMATIC OF THE PHOTONIC CRYSTAL MICROCAVITY LASER AND GENERIC EPILAYERS. ... 32
FIGURE 11. SCHEMATICS OF THE GROWN SAMPLES ... 37
FIGURE 12: PHOTOLUMINESCENCE DATA FOR GROWN STRUCTURES ... 39
FIGURE 13: GROWN STRUCTURES AND THEIR TRANSVERSE FUNDAMENTAL MODE DISTRIBUTIONS. ... 41
FIGURE 14: L-I CURVES FOR THE PHOTONIC CRYSTAL MICROCAVITY LASER. ... 45
FIGURE 15: MASK VIEWS WITH VARYING ZOOM LEVELS. THE RED OVALS INDICATE THE REGION SHOWN IN THE FOLLOWING ZOOM LEVEL. A.) THE ENTIRE STEP AND REPEAT MASK INCLUDES 36 IDENTICAL DIES, B.) EACH DIE CONSISTS OF 234 LASERS OF VARYING DIMENSIONS AND MANY DIAGNOSTICS. C.) EACH UNIT CELL ON THE DIE CONTAINS 12 LASERS AND ACCOMPANYING CONTACTS. D) AN ARRAY OF 6 LASERS EACH SEPARATED BY 30µM. E.)EACH LASER REQUIRES 8 MASKS TO FABRICATE. ... 49
FIGURE 16: SCHEMATIC OF A SINGLE STRIPE LASER DIAGNOSTIC. ... 50
FIGURE 17: MASK LAYOUT OF STRIPE LASER WITH INTEGRATED PASSIVE SECTION ... 50
FIGURE 18: THE INTEGRATED DIAGNOSTIC DETECTOR ... 51
FIGURE 19: FABRICATION SEQUENCE FOR THE ELECTRICALLY ACTIVATED MICROCAVITY LASER AND DIAGNOSTIC STRIPE LASER. STEPS 8-10 WITH A DOTTED LINE AROUND THEM ARE ONLY REQUIRED TO FABRICATE DIAGNOSTIC STRIPE LASERS BEFORE E-BEAM LITHOGRAPHY, OR IF ONE USES FOCUSED ION BEAM LITHOGRAPHY. ... 55
FIGURE 20: A) THE BAND DIAGRAM AND POTENTIAL BARRIER ASSOCIATED WITH THERMIONIC EMISSION. B) THE BAND DIAGRAM AND POTENTIAL BARRIER ASSOCIATED WITH CARRIER TUNNELING. ... 56
FIGURE 21: METAL FEATURES AFTER STEPS 1-2. A.) A UNIT CELL CONTAINING 6 ACTIVE REGIONS. B.) ALIGNMENT MARKS C.) VERNIER ALIGNMENT MARKS AS VIEWED WITH A 50X OBJECTIVE. EACH LINE IS 1.5µM WIDE WITH A MINIMUM SPACING OF 1.5µM BETWEEN EACH LINE. ... 59
FIGURE 22: PHOTONIC CRYSTAL LASER FEATURES AFTER REMOVING THE *P*-TYPE MATERIAL. A.) THE ACTIVE AREA OF A LASER WITH THE PATTERNED *P*-TYPE BEAM DEFINED. B.) A UNIT CELL DEPICTING A TOTAL OF 12 ACTIVE AREAS. ... 61
FIGURE 23: EXAMPLES OF METAL ADHESION PROBLEMS AFTER WET-ETCH. A.) ROWS OF STRIPE LASERS WITH AN INTEGRATED LOSS-SECTION. METAL IS ONLY ATTACHED TO THE LARGE CONTACTS WHICH WERE PROTECTED BY PHOTORESIST. B.) VERNIER ALIGNMENT MARKS HAVE MISSING PIECES WHICH APPEARED TO HAVE PEELED OFF FROM THE UNDERLYING GAAS MATERIAL. C.) THREE ROWS OF STRIPE LASERS WITH THE 3RD ROW COMPLETELY MISSING. ... 62
FIGURE 24: ANNEALED METAL CONTACT THAT WAS USED TO FABRICATE THE SELF-ALIGNED RIDGE WAVEGUIDE. THE LACK OF SURFACE MORPHOLOGY IS PROBABLY DUE TO THE ANNEAL. ALSO, THE SURFACE ROUGHNESS OF THE RIDGE LEADS TO AN UNACCEPTABLE RIDGE WAVEGUIDE. ... 63
FIGURE 25: CROSS-SECTIONAL VIEW OF AN ALTERNATIVE METHOD TO FORM THE RIDGE OF THE STRIPE LASER WITHOUT USING METAL AS A WET-ETCH MASK. THIS METHOD DOES NOT REQUIRE ANY DRY-ETCHING, BUT DOES REQUIRE GOOD ALIGNMENT DURING THE RE-PATTERNING OF MASK 1. IT IS IMPORTANT TO REALIZE THAT ONE MUST APPLY AND PATTERN MASK 2 BEFORE WET-ETCHING THE GAAS-BASED MATERIAL IN ORDER TO FORM THE P-TYPE BEAM OF THE PHOTONIC CRYSTAL LASERS. . 64

Figure 26: Electron-beam field alignment marks included in the mask design that were formed during second metal deposition. 65
Figure 27: Unit Cell after steps 4-5. Compare to Figure 15(c). 66
Figure 28: Electron-beam lithography process leading up to the etching of the submicron feactures. Some layer colors are made partially transparent to reflect actual visibility. 69
Figure 29: The ridge laser with accompanying fabrication sequence. 71
Figure 30: Grown Ridge Lasers and Acommpanying PL 73
Figure 31: Sample VA36 before the second contact deposition. Stripes widths are as small as 1.5μm 74
Figure 32: L-I curves for a ridge laser 75
Figure 33: Boundary conditions for an optical cavity. 77
Figure 34: Top view of a photonic crystal laser utilizing adiabatic tapers 78
Figure 35: 2 variations of a 3D mirror confined microcavity laser 80

Chapter 1.

Introduction

1.1. Motivation

Silicon microelectronics has had an undeniable impact on our society. Large scale integration technologies have enabled the creation of low cost, high performance computer chips that are present wherever electronic data resides. However, silicon electronics is approaching fundamental performance limits. Many of the problems associated with silicon electronics originate from the metal wires used for interconnects [1]. In particular, wires are inherently resistive and as their cross sections shrink, their resistance increases. Associated with resistive losses is heat which can adversely affect the performance of other devices on the integrated circuit (IC). Also, as dimensions shrink and modulation speeds increase, the metal wires must be treated as transmission lines. Inherent to transmission lines is capacitance per unit length which affects the speed that information can be transmitted. As the distance between wires decrease, the wires can act like miniature antennas sending and receiving unwanted data, a process known as cross-talk.

By transmitting information optically many of the problems associated with metal wires can be avoided. Simple impedance arguments show that optical photons can transmit information with less energy than electrons [2]. Optical fibers are already the primary data path in long distance telecommunication systems. In wavelength division

multiplexing (WDM), many optical signals of different wavelengths are transmitted through a single fiber. This parallelism can not be achieved with electrons which are charged carriers. Thus, the goal of integrated optics is to extend optics' success in long-haul telecommunications, to short-range communication systems such as microprocessors where integrated optics can act as a data link between components on a single chip, or a communication link between chips. However, the exact architecture for implementing photonic integrated circuits (PIC) has not been determined. In order to compete with silicon electronics, PIC's must be small and fast while consuming little power. These PIC's will require a light source such as a laser. The laser must also be compact, efficient, and be able to run at high speeds.

A microcavity laser satisfies all of these constraints by its nature. By confining light to wavelength scales, microcavity lasers are superior to large lasers in almost every way with the exception of output power. This thesis focuses on the fabrication and design of a microcavity laser that is well suited for integrated optics. The laser is specifically designed to be electrically activated and emit light in-plane. A smaller optical cavity means that light reflects off the cavity walls more frequently necessitating high reflectivity mirrors to avoid excessive loss. Since perfect reflectors do not naturally exist in the optical regime, lithography-defined reflectors called photonic crystals are utilized in the design of the microcavity laser.

1.2. Photonic Crystals

A photonic crystal (PC) is a periodic arrangement of dielectric material [3]. A unique property of photonic crystals is that they exhibit a photonic bandgap, a range of

frequencies in which light can not propagate within the photonic crystal. Photonic crystals fabricated from semiconductor material are particularly desirable, because the PC can be fabricated using standard microelectronic fabrication techniques, and can thus be incorporated with other optical components on a single chip. Photonic crystals fabricated using such techniques are usually limited to one-dimensional and two-dimensional arrangements of rods or holes on a semiconductor substrate. The planar nature of conventional microelectronic fabrication techniques makes it difficult to create structures exhibiting a photonic band-gap in three dimensions, although researchers are finding new ways to create three-dimensional photonic crystals [4].

To create a photonic crystal laser, two criteria must be met. First a resonator must be created and secondly, the laser must have sufficient gain to overcome the losses associated with the resonator[1]. A defect can be incorporated into a photonic crystal by increasing or decreasing the size of a particular rod or hole, or by eliminating one of the rods or holes all together. The use of a defect breaks the symmetry of the optical lattice and creates areas or sites where once forbidden modes can propagate or oscillate depending on the situation. Hence, the defect within the photonic crystal acts as a resonator. In a well designed oscillator, the resonant frequency of a mode associated with a defect lies within the range of forbidden frequencies, the photonic band gap (PBG), of the surrounding photonic crystal. By including an optical gain medium within the defect, one can exploit the high reflectivity of the surrounding photonic crystal and the small modal volume to create a very efficient laser with photonic crystal mirrors [5].

---

[1] For microcavity lasers the gain can actually be much smaller than the loss and one can still observe lasing. This phenomenon will be explained later in the thesis.

1.3 Overview

By utilizing a defect with two one-dimensional photonic crystal mirrors to trap light in a cavity with dimensions on the scale of a wavelength, a microcavity laser can be created. The small size of the laser conserves space and leads to a low threshold power. The laser will be designed using simulation software, and will be fabricated using standard semiconductor lithographic and pattern transfer techniques. Simple ridge lasers will be fabricated to test the quality of the starting epitaxy material.

This thesis discusses the various aspects of creating a microcavity, electrically-activated photonic crystal laser. Chapter 2 presents the basics of lasers with emphasis on the use of microcavities. Chapter 3 discusses the design and the simulations of the microcavity laser. The initial fabrication results are shown in Chapter 4. Finally, Chapter 5 summarizes the thesis and presents future avenues for investigation.

Chapter 2.

Laser Basics

2.1. Background

The control afforded by microelectronic fabrication techniques allows the creation of one and two dimensional photonic crystals that are composed of semiconductor materials as well as the creation of semiconductor optical and electrical devices. Semiconductor lasers are particularly desirable because they are relatively small, and can be integrated with other optical components such as modulators and detectors on a single chip. This section provides a brief background of semiconductor laser technology, and explains the subtleties of spontaneous emission, a key process in microcavities.

2.2. Semiconductor Lasers

In general, a laser requires an emitting medium and optical feedback. A material with an indirect bandgap, such as silicon can not efficiently emit light while conserving momentum, so various direct bandgap III-V materials are used for semiconductor lasers. The most common III-V semiconductors include various alloys of indium, gallium, aluminum, arsenic, phosphor and nitrogen. A medium can emit light through either spontaneous or stimulated emission, and it can absorb light through stimulated absorption as shown schematically in Figure 1. In stimulated emission, a photon causes an electron

and hole to recombine and emit a second photon. The emitted photon is in-phase with the original photon, so that two identical photons result. Conventional lasers rely on photon creation by stimulated emission for a coherent source of light. Conventional lasers are defined in this thesis as lasers whose optical cavity dimensions are larger than the emission wavelength. Optical feedback is necessary so that a generated photon can return to the emitting medium in order to generate more photons through stimulated emission. Optical feedback is usually achieved by placing mirrors, such as photonic crystals, around the emitting medium, so that light is confined within the cavity.

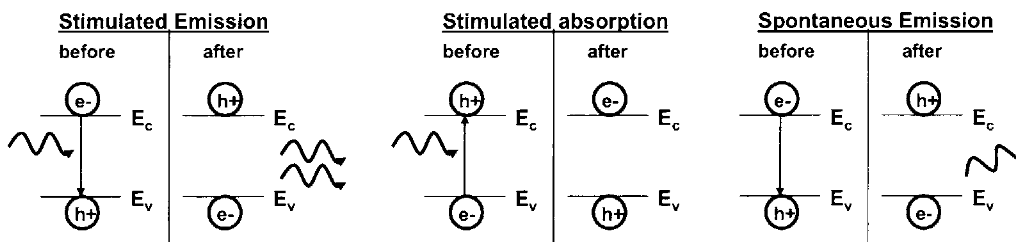

Figure 1: Light-matter interaction processes.

To achieve lasing, the rate of photon emission into the lasing mode must exceed the rate of stimulated absorption. Therefore, in a semiconductor laser, the number of available electrons in the conduction band must be in excess of a threshold value so that the probability of emission is larger than the probability of absorption. This is accomplished by means of pumping the semiconductor laser from an external source. Pumping excites electrons into the conduction band from the valence band leaving behind holes in the empty states. Since electrons and holes both obey Fermi-Dirac statistics, excited electrons will occupy the lowest energy states in the conduction band, while holes will occupy the highest energy states in the valence band. Pumping leads to a band

diagram in the active area as shown in Figure 2 whereby the average energy required for absorption is larger than the average energy released in emission [6]. The electron and hole energies are characterized by their quasi Fermi levels, E_{fc} and E_{fh} respectively. The quasi Fermi level is the energy at which the carrier occupation probability is 0.5. When $E_{fc}-E_{fh} \geq h\upsilon$ where $h\upsilon$ is the energy of the photon that is being emitted, the probability of emission is larger than the probability of absorption, so that the material exerts a net gain and is said to be population inverted [7].

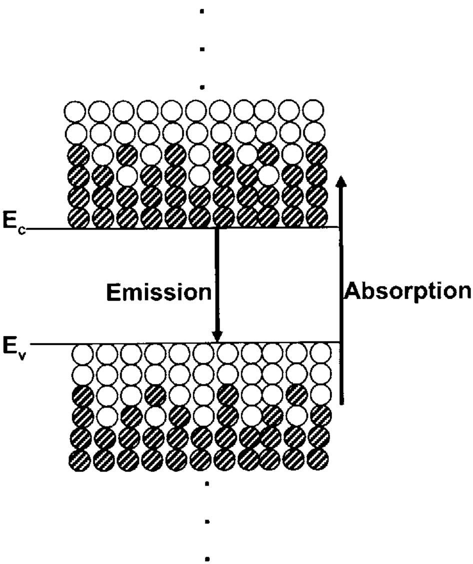

Figure 2: A simplified band diagram of the active region due to pumping. Shaded circles represent filled states or electrons, while white circles are empty states, or holes. Concepts taken from [6].

2.3. Diode Lasers

The simplest form of a semiconductor laser is a *p-n* diode with mirrors on either end as shown in Figure 3. A *p-n* junction diode is used because it is the simplest known semiconductor device in which large concentrations of electrons and holes reside in close proximity to each other at the same time, so that recombination and thus emission of radiation is likely to occur.

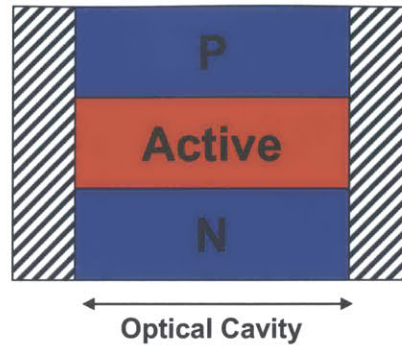

Figure 3: A simple edge emitting diode laser with mirrors on the side

Almost all modern diode lasers are based on separate confinement heterostructure quantum well designs. The quantum well is formed by surrounding a small bandgap active material with a barrier material that has a larger bandgap. The quantum well confines electrons and holes to a small volume preventing their diffusion across the *p-n* junction and hence increases the possibility of radiative recombination. Quantum wells also reduce the volume of the gain region meaning that fewer net carriers need to be present to achieve a given carrier density. This reduces the threshold current and also reduces the laser's turn on time by increasing the differential gain. However, a low volume gain region has its shortcomings. Physically, a smaller active medium volume means less of the electromagnetic mode overlaps the gain region decreasing the effective gain per unit length. To counteract this reduction in modal gain, lower index cladding regions are placed on either side of the active material to separately confine the electromagnetic mode to the gain region [8]. The cladding regions also ensure that the optical cavity is large enough to contain an electromagnetic mode of the desired wavelength.

2.4. The role of spontaneous emission in microcavity lasers

Many of the outstanding properties of microcavity lasers, such as high efficiency, small threshold current and high bandwidth, result from the nature of spontaneous emission in a wavelength-sized cavity. In particular, the spontaneous emission rate, the lasing mode coupling, and the emission pattern, can all be modified by including a medium in an optical microcavity. Figure 4 shows how the emission intensity distribution of an x-oriented dipole is affected by a cavity [9]. The cavity is created by placing perfect mirrors at $x = \pm L/2$. When the frequency of the dipole, ω, is such that the wavevector, k, equals $\omega/c=\pi/L\equiv k_c$, the cavity is tuned to the emission frequency of the dipole and one observes an enhanced emission intensity distribution as shown in Figure 4(b). Thus, the usual description of spontaneous emission characteristics, being an intrinsic property of a particular medium, is no longer accurate, because the atom and the field become a coupled system and can not be considered separately. The study of this coupling, known as cavity quantum electrodynamics (QED), can be complex. Therefore, the purpose of the following sections is to give a qualitative physical description of cavity QED and its application to microcavity lasers.

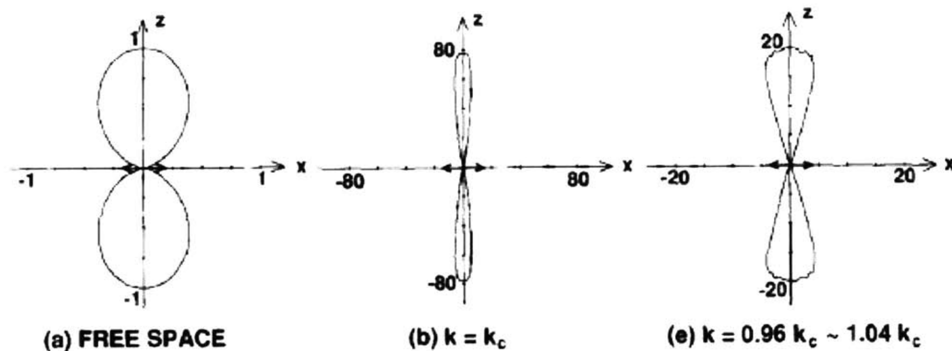

Figure 4: Emission intensity distribution of an x-oriented dipole in a) Free space, b) $\lambda/2$ one dimensional cavity with frequency corresponding to cut-off, and c) $\lambda/2$ one dimensional cavity below cut-off. Figures and concepts from [9].

2.4.1. Motivation for the Optical Microcavity

In conventional lasers where most, if not all, of the optical cavity dimensions are much larger than the emission wavelength, spontaneous emission is primarily an energy loss process. In conventional lasers, the large dimensions result in many possible electromagnetic modes. Thus, spontaneously-emitted photons are unlikely to occupy the lasing mode[2]. For this conventional case, spontaneous emission consumes carriers without emitting photons into the lasing mode, the mode that experiences the largest net optical gain, and wastes pump energy. Since spontaneous emission is usually the largest carrier loss process below threshold, by increasing the proportion of photons spontaneously emitted into the lasing mode, the laser is more energetically efficient.

In microcavity lasers, the optical cavity dimensions are on the order of an optical wavelength resulting in much fewer possible optical modes, and thus a higher probability of coupling into the lasing mode assuming proper cavity tuning as shown in Figure 5. The coupling probability is quantified in the spontaneous emission factor, β_{sp}, which is the fraction of photons emitted into the lasing mode. Inclusion of a gain medium in a microcavity resulting in a large β_{sp} improves the performance of a laser. The laser is more energy efficient and exhibits a smaller threshold current (which will be described once a more uncommon definition of threshold is introduced). Microcavity lasers have much smaller turn-on times [10]. Below threshold, the light intensity increases from spontaneous emission, so by increasing the spontaneous emission *rate* into the lasing mode, the laser turns on faster once an input current is applied. Microcavity lasers also

[2] Although photons are particle-like in that photons exchange discrete quanta of energy with atoms, photons are wave-like in that photons must fulfill the boundary conditions of their surroundings [15]. Consequently, photons can only exist by occupying a particular electromagnetic mode whether it be a free-space or a resonant mode. Thus, one can never identify the exact location of a photon.

exhibit shorter turn-*off* times due to a reduced photon lifetime within the cavity that is caused by a higher mirror loss rate. Finally, since spontaneous emission into non-lasing modes ultimately sets the noise limit of a laser, microcavity lasers have been shown to have less noise both theoretically [11], and experimentally [12].

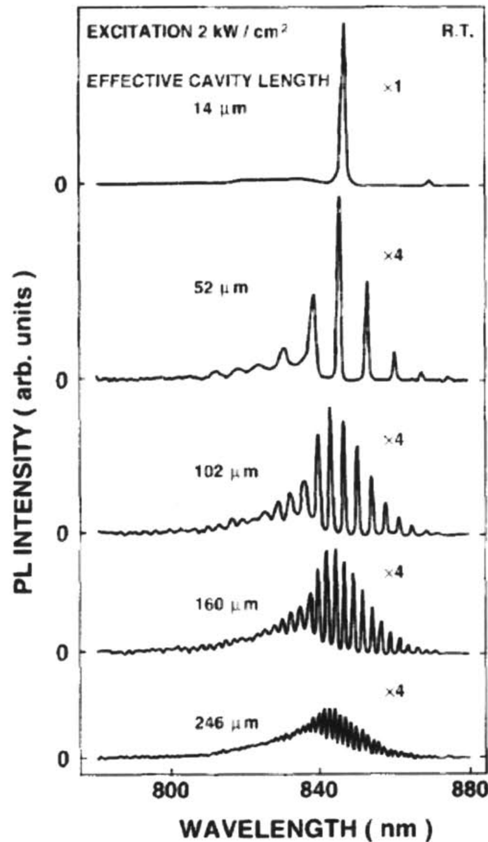

Figure 5: Photoluminescence spectrum of Fabry-Perot cavities of different axial lengths. The light is detected from the cavity axis. As the dimensions of the cavity decreases, light is more likely to be emitted into the lasing mode. Figure is taken from [9].

2.4.2. The quantum-mechanical view of spontaneous emission: Vacuum fields

As mentioned from the simple mode counting arguments, spontaneous emission both "seeds" and "bleeds" the optical resonator [13]. However, the previous section did not explain how an atom can "feel" the effects of it surroundings when placed in a microcavity so that the "seeding" of light into the lasing mode is more potent. The

previous section also did not explain such effects as lasing without population inversion, reversibility which thwarts the carrier "bleeding" process, or spontaneous emission enhancement/inhibition where the rate of spontaneous emission into a mode is altered. The goal of this section is to explain these phenomena by giving a physical picture of how atoms and fields are inherently coupled, and how this coupling becomes noticeable in a microcavity. The final conclusion will be that spontaneous emission can be tailored and controlled, and hence is not very spontaneous at all.

Vacuum Fields in Cavity QED

Much like a golf ball at the top of a hill, an electron occupying an excited energy level of an atom, or lattice, will remain there until another system interacts with it, even though a lower energy level is energetically favorable [14]. In the case of spontaneous emission, an electromagnetic field mode corresponding to the atom's transition frequency must be present to induce an emission event. This might appear contrary to the description of spontaneous emission offered by Einstein, where he showed that the spontaneous emission rate, R_{sp}, is proportional to the number of excited atoms and is independent of the number of photons through the following equation [15]:

$$R_{sp} = \left.\frac{dN}{dt}\right|_{spont.} = -A_{21} N \tag{1}$$

where A_{21} corresponds to the spontaneous emission probability (sec^{-1}), and N is the number of excited atoms. If the above equation is indeed true, then even without photons present, spontaneous emission will still take place giving the false impression that a medium does not require any outside influence in order to spontaneously emit a photon.

However, the Einstein coefficient, A_{21}, contains information about the outside world, and in particular, the effect of vacuum fields which exist even in the absence of "real" photons [15]. The vacuum, or zero-point, field is responsible for half of the spontaneous emission rate [15] meaning,

$$A_{vac} = \frac{1}{2} A_{21} \tag{2}$$

where A_{vac} is the transition probability per unit time due to the vacuum field. The vacuum field is the electromagnetic field present in all space in the absence of photons. Its existence is verified when one treats an electromagnetic field mode quantum mechanically and quantizes it in terms of creation and annihilation operators [15]. Realizing that a monochromatic field mode is mathematically equivalent to a harmonic oscillator, one arrives at the following equation for the oscillator energy levels.

$$E_n = \hbar \omega \left(n + \frac{1}{2} \right) \tag{3}$$

Where n is an eigen-number representing the number of photons present in the mode oscillating with angular frequency, ω. The above equation reveals that even without photons present (n=0), there is still a finite energy of $\frac{1}{2}\hbar\omega$ present in the mode. This is the zero-point energy of the harmonic oscillator which must be attributable to a field with zero-mean, (otherwise the intensity could be viewed with a detector) yet with non-zero fluctuations in time [13]. These vacuum fluctuations, or vacuum fields, are what induces spontaneous emission. Accounting for the infinite number of frequency possibilities, one arrives at the conclusion that the vacuum field can be thought of as an infinite "bath" of energy [15]. Nonetheless, since energy is relative, one can mathematically set the vacuum energy of a mode to zero although its affects cannot be eliminated[3].

However, the vacuum field only accounts for half of the spontaneous emission probability, the other half comes from the radiation's reaction field, a classical phenomenon [16], which is the reaction of the atom to its own oscillations, similar to the recoil of a gun. Thus, for the radiation reaction component of A_{21} one can write,

$$A_{rr} = A_{vac} = \frac{1}{2} A_{21} \tag{4}$$

Addition of the radiation reaction and vacuum component preserves the total spontaneous emission rate given in equation (1). Interestingly, the radiation reaction field is the reason why there is no such thing as spontaneous absorption as the radiation reaction field can only induce downward transitions; it exactly cancels the upward transitions of absorbed vacuum field quanta [15].

With the existence and role of the vacuum field confirmed, spontaneous emission is simply stimulated emission under the influence of the vacuum field [17] meaning that a spontaneously emitted photon is in phase with the perturbing vacuum field. So in reducing the number of vacuum states in a microcavity, one simultaneously eliminates spontaneous emission into unwanted modes. Thus, the vacuum field couples the cavity to the medium. By properly designing a cavity, one can judiciously eliminate vacuum field modes and thus carrier loss by spontaneous emission into non-lasing modes. Hence, mirrors play a different role in microcavity lasers than conventional lasers. Rather than providing optical feedback for stimulated emission, the mirrors prevent unwanted vacuum field modes from inducing spontaneous emission into unwanted optical modes.

If one embeds a narrowband medium, such as quantum dots or quantum boxes in a properly designed microcavity, not only is the probability of coupling into the lasing mode increased, the spontaneous emission *rate* into the lasing mode as compared to free

[3] Another effect besides spontaneous emission is the Casimir Effect [15] whereby two conducting plates are attracted to each other.

space is enhanced [18]. This phenomenon, known as the Purcell Effect [19], can be explained with the vacuum field as follows: By reducing both the number of vacuum states and emission bandwidth of the medium, a resonance condition between the vacuum field and the emitting medium is created, where both systems oscillate at the same frequency. In the case of a narrowband medium in a large cavity, the resonance condition is not met, because vacuum fields of the correct frequency, but associated with non-lasing modes, can induce emission thereby reducing the instances per second (rate) at which atoms emit into the lasing mode. Conversely, an emitter with a large spectral width in a microcavity can only exhibit a modest Purcell Effect, because the vacuum mode is still unlikely to find an atom in a state corresponding to the correct transition frequency[4]. Minor Purcell enhancement is possible though, if the vacuum modes of the lasing frequency are reduced, so that only the cavity mode can induce spontaneous emission.

To take the analysis one step further, if a narrowband medium is embedded in a single mode cavity having negligible losses, the coupling between an atom and the field becomes noticeably pronounced. In the strong coupling regime, energy is continuously exchanged between the atom and the field [20]. With only one vacuum mode in the emission linewidth of the atom, the atom can only emit into the cavity mode. However, once the photon is generated, it resonates in the nearly lossless cavity, only to be coherently absorbed by the atom. Instead of gradually decaying into a lower energy state, the atom oscillates between excited and ground states at the Rabi frequency. Thus, by properly engineering a cavity, spontaneous emission is a completely reversible and controllable process. Rather than quanta of light flowing from the vacuum field into the source field, it is periodically exchanged between the two [21]. This periodic exchange

[4] This situation will result in an increase of the spontaneous emission factor though, because many vacuum modes corresponding to non-lasing frequencies have been eliminated.

reveals the nature of photon generation and annihilation. A photon is never generated or annihilated; it only transitions out of and into the vacuum field [15]. It is in the strong coupling regime that these affects are apparent and new states of light can be generated [12], making the engineering of quantum computers a possibility.

2.5. Other Photonic Crystal Lasers

The potential for creating efficient microcavity lasers using photonic crystals has been recognized ever since the possibility of a photonic crystal was first reported [5]. Since then, several groups have reported lasing in photonic crystal lasers. In fact, since the Distributed Bragg Reflector (DBR) mirror stack in a Vertical-Cavity Surface-Emitting Laser (VCSEL), is essentially a one-dimensional photonic crystal, photonic crystal lasers are not necessarily a new technology [3]. Indeed, a microcavity oxide-confined VCSEL has yielded a record low threshold current of just 8.7μA [22,23]. VCSELs naturally have good thermal management, so microcavity VCSELs can achieve continuous-wave (CW) operation. However, since VCSELs emit light vertically, away from the plane of the chip, their integration with other optical components is very difficult. Distributed Feedback (DFB) and DBR lasers emit in-plane and are known to have low noise and single mode lasing. However, these lasers usually have threshold currents in the milliampere range with no references found for DFB or DBR lasers requiring microamp threshold currents. Thus, a niche exists for low threshold edge-emitting lasers. To construct a low threshold edge-emitting laser, light can be confined laterally by use of photonic crystal mirrors. The remainder of this section focuses on low-threshold photonic crystal lasers.

The difficulty of making an electrical contact to a microcavity without injecting carriers into unwanted portions of a device causes electrically-activated photonic crystal lasers to be less common than their optically-pumped counterparts. However, optically-pumped lasers have demonstrated microcavity proof-of-concepts such as low threshold powers and high speed operation. For instance, Altug *et al* [24] has demonstrated optically-pumped photonic crystal lasers with a delay time of 1.5 ps allowing the direct modulation of a photonic crystal laser at rates approaching the THz range. The photonic crystal laser, consisting of a single defect in a photonic crystal membrane, is shown in Figure 6. Although the photonic crystal membrane was cooled to obtain these results, the ultra-small cavity could enable high speed direct electrical modulation of the laser.

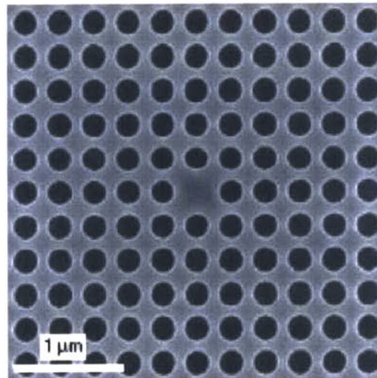

Figure 6: Top view of a single defect photonic crystal laser [24]. The defect is performed by removing a single hole from a surrounding photonic lattice.

An electrically-activated laser was demonstrated by Park *et al* [25] with a threshold current of just 260µA operating at room temperature. To tackle the problem of making electrical contact to a microcavity resonator, the two-dimensional photonic crystal slab sits on a post of semiconductor material. Electrical injection is limited to the area of the resonator by means of the *p-i-n* junction which limits the carrier flow to other regions of the laser to length scales on the order of a diffusion length. Surface

recombination at the edges of the photonic crystal holes probably limits the threshold current. The free standing structure might also be awkward to integrate with other components on a chip. The electrical drive current was pulsed so CW lasing was not demonstrated. Finally, because the photonic crystals strongly confine the light in the plane of the chip, the laser is surface emitting [26], although the authors do not explicitly state the laser's emission direction.

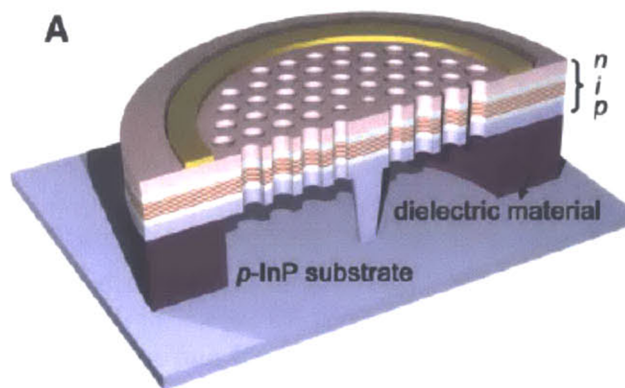

Figure 7: Electrically-activated photonic crystal laser demonstrated in [25].

Happ *et al* demonstrated a coupled cavity photonic crystal laser, shown in Figure 8, with a threshold current of 15mA using coupled cavities to form a waveguide for the light [27]. The high threshold current is caused by the lateral diffusion of carriers to regions outside of the coupled cavity waveguide. The coupled cavity waveguide photonic crystal laser does achieve electrical activation and continuous wave (CW) lasing with a coplanar output. However, the lasers are composed of around 40 microresonators and are 155μm in length, much larger than other photonic crystal-based lasers.

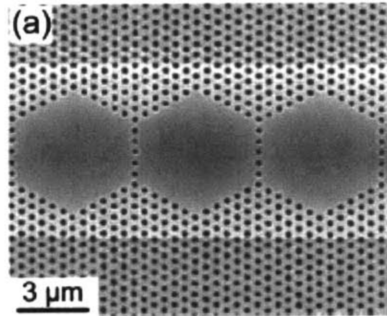

Figure 8: Coupled cavity photonic crystal laser [27]. The hexagonal features are microresonators within a surrounding PBG lattice. Shown here are 3 of 40 total microresonators.

Zhou *et al* reported an electrically-activated laser-like structure that exhibited a soft-threshold characteristic that is the result of a high spontaneous emission factor [26]. A single defect is incorporated into a photonic crystal and a distributed Bragg reflector stack is used to isolate the optical mode from the bottom contact and the substrate. A schematic of the device and the light-current performance of the device are shown in Figure 9. In pulsed operation, a "soft" threshold current of 300μA is observed with a maximum output power of 14.4μW. The soft transition at threshold is due to a large spontaneous emission factor of β≈0.06. Since the carriers must traverse around many-lithography defined holes to reach the active region, the device suffers from a large amount of surface recombination at the hole edges. Also, since the photonic crystals confine light in-plane, most of the light leaks out vertically and not in-plane.

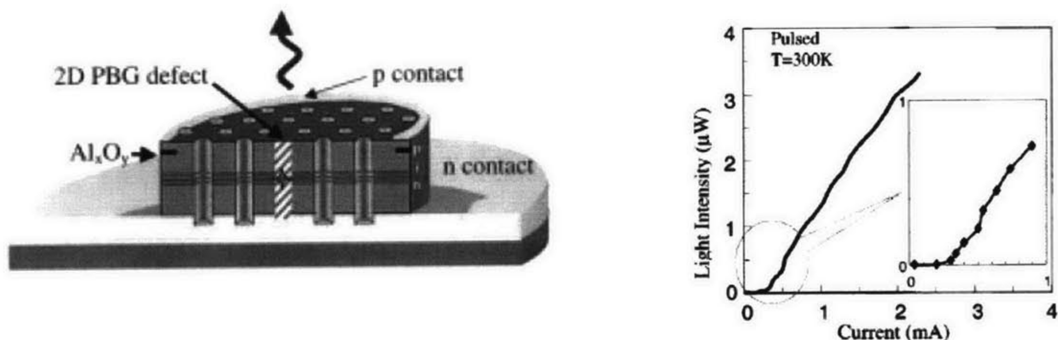

Figure 9: Schematic and output characteristics of the laser described in [26]. The device is isolated from the substrate by an oxidized bragg mirrors stack. The oxidation front is stopped just before the defect, so that current can be injected from the bottom contact. The soft threshold is shown in the inset of the L-I curve.

Chapter 3.

Design and Simulations

3.1. Design Concept

From the reports in the literature, there is no work describing electrically-activated, edge-emitting microcavity lasers. A fundamental problem with the design of electrically-injected, edge-emitting, microcavity lasers is the placement of the contacts. The difficulty lies in positioning the contacts, so that they only inject current into the microcavity without interfering with the emitted light. The design of the laser investigated here accomplishes electrical injection into a microcavity through the use of crossing semiconductor beams and an undercut. Another problem with edge-emitting lasers is the removal of the active material from the passive output waveguide, while still maintaining a microcavity. The crossing-beam design presented below accomplishes this by selective etching of the active material from the passive output waveguide. A schematic of the laser and a simplified schematic of the epilayers for one particular device used in this thesis are shown in Figure 10.

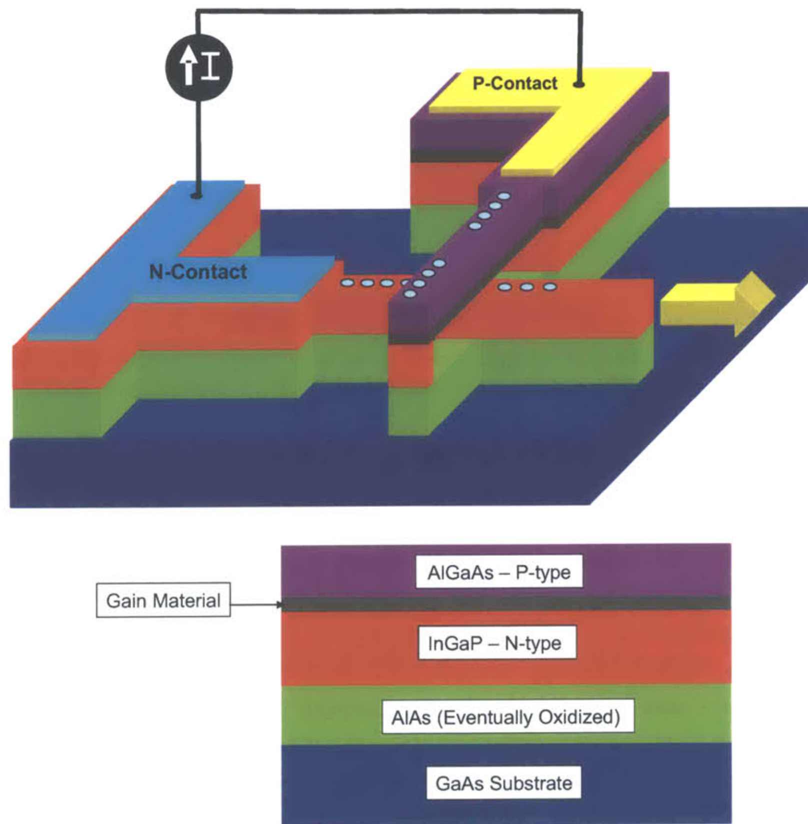

Figure 10: Schematic of the photonic crystal microcavity laser and generic epilayers.

The electrically-activated photonic crystal laser uses two crossed beams of semiconductor material to create a microcavity. Holes are injected into the microcavity from the top *p*-type beam and electrons are injected from the bottom *n*-type beam. The crossing of the two beams defines the active area where the carriers ideally recombine radiatively in the gain material residing within the top beam. Light generated in the gain material is coupled into the bottom, output waveguide (shown in red in Figure 10). The photonic crystals, which act as mirrors, are formed by patterning holes into each beam except where they cross. The lack of holes creates a defect within each beam resulting in a highly efficient resonator for frequencies residing within the photonic bandgap. Fewer holes are patterned in one direction of the bottom waveguide, so that the emitted light

will be preferentially transmitted into the passive output waveguide in this direction. Light is confined by index confinement in the vertical direction and by the photonic bandgap in the axial direction.

The *p* and *n*-type regions are electrically isolated everywhere except in the active region by the use of an undercut which removes the *n*-type material underneath the regions of the top beam that are patterned. Without performing this undercut, the entire device would function as a *p-i-n* diode and the benefit of forcing the electrons and holes to recombine only in the active region would be lost. The undercut also reduces the optical cavity volume by removing material that could otherwise contain part of the optical mode. As mentioned in Chapter 2, a reduced cavity volume has many effects including a reduction of the threshold current.

Thermally-oxidized AlAs is formed underneath the bottom waveguide to further confine carriers and photons to the desired areas. Oxidized AlAs (Al_xO_y) serves as an insulator so that a current path does not exist between the contacts via the substrate. This parallel current path might lead to an unreasonably high threshold current if the resistive path through the substrate is low. The oxidized AlAs also has a low refractive index (1.55) which prevents the optical mode from leaking into the high refractive index substrate.

The microcavity photonic crystal laser is well suited for integrated optics for many reasons. The laser is electrically-activated eliminating the need for a separate pump laser and the difficulty of focusing an optical pump beam on a microcavity-sized structure. The photonic crystal laser is both practical and efficient; both the active and cavity volume are small which leads to a small threshold current, high efficiency, high

speed, and low noise. The laser has a relatively small footprint, which conserves valuable chip real-estate. Finally, the laser's output is fed directly into an in-plane optical waveguide eliminating the need for couplers thus easing integration of the laser with other components. Figure 10 shows how the output light beam leaves the microcavity in the lower waveguide in the direction of the fewest holes, in this case, three holes.

3.2. Layered Structure Design

Many considerations were taken into account when designing the thickness and composition of the epilayers. In an initial design, the output waveguide rested on the absorbing active material making it incapable of guiding light with low loss. In later designs, the laser structure was "flipped" so that the output waveguide resides just above the oxidized AlAs layer and the active material is removed from above the output waveguide.

In the initial microcavity laser designs, the top beam was referred to as a waveguide, because it was thick enough to support a guided mode. In the current design, the dimensions of the top AlGaAs cladding layer were reduced, so that the upper-beam would be unable to support any optical mode of the light that is being generated by the active medium. A trade-off is incurred however, because the top beam also contains the gain medium. If an insufficient amount of light resides within the top beam, the modal overlap with the gain material will be insufficient to support lasing. If too much of the optical mode overlaps the gain material, the generated light will not couple into the output waveguide as usable light. Thus, optical simulations were carried out to ensure that the optical mode overlaps both the active medium and the output waveguide. These

modal simulations (section 3.2.1) were used to determine the thickness of the AlGaAs cladding and the output waveguide.

The maximum vertical thickness of all the grown layers could not exceed 1.2μm due to the maximum thickness (~1.8μm) of the Clariant AZ5214 photoresist that was used in the fabrication the laser. This constraint limits the thickness of the underlying aluminum oxide layer and hence the AlAs layer. Ideally, the Al_xO_y layer should be quite thick (~1μm) in order to prevent light from coupling into the GaAs substrate. In the first generation of grown wafers, sample VA28, the AlAs thickness was 1.0μm, but during the fabrication of the microcavity laser, an AlAs thickness of 1.0μm was determined to be too thick to insure adequate photoresist coverage. Two new generations of samples (VA34 and VA35) were grown with an AlAs thickness of 0.5μm. The latest generations incorporated many other changes which are explained below.

The first generation, sample VA28, included an InGaAlP-based output waveguide with a high index, dilute waveguide core composed primarily of InGaP interspersed with thin GaAs layers. The high index core serves to "pull" light down into the output waveguide from the upper active region. Although InGaAlP provides an output waveguide whose index of refraction is slightly lower than $Al_{0.5}Ga_{0.5}As$, InGaAlP is difficult to etch using the reactive ion etchers at M.I.T. Subsequent samples (VA34 and VA35) used a thick layer of InGaP for the output waveguide material.

Phosphide-based material was used as the output waveguide primarily for two reasons. First, materials such as InGaP or InGaAlP are known to have less optical loss than GaAs or AlGaAs [28]. Secondly, the significant etch selectivity between phosphide-based and arsenide-based materials is necessary for the undercut step.

Schematics of the final grown wafers are shown in Figure 11. All of the wafers were grown in the Veeco GEN 200 Molecular Beam Epitaxy (MBE) system in the Nanoprecision Deposition Lab. MBE can provide high crystalline quality III-V epitaxial films of precise thicknesses.

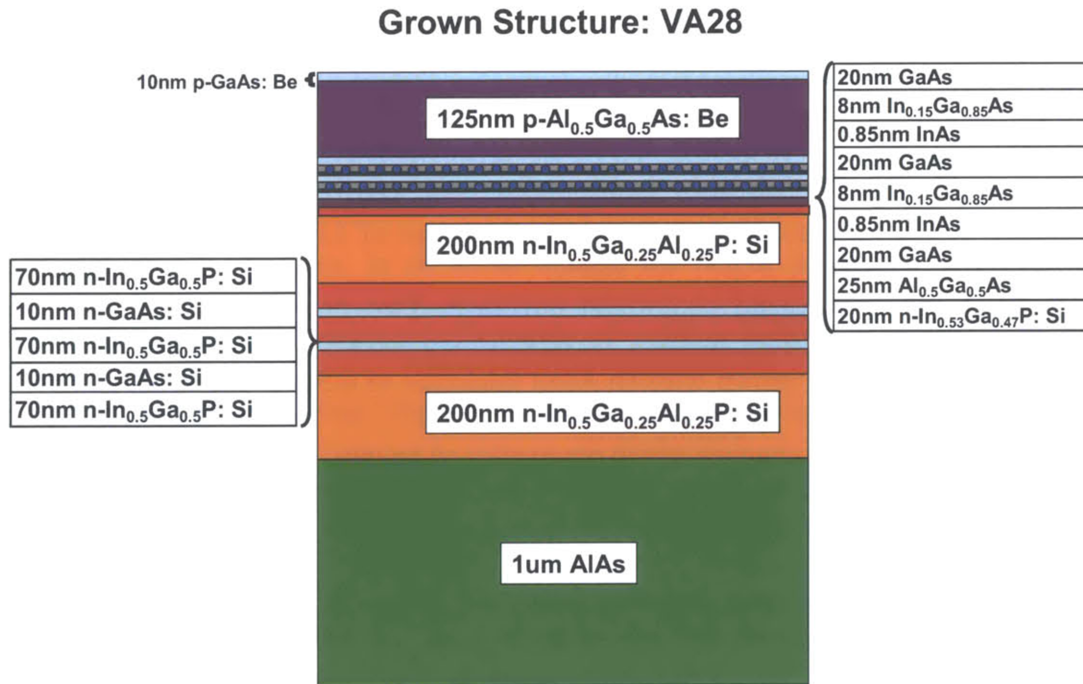

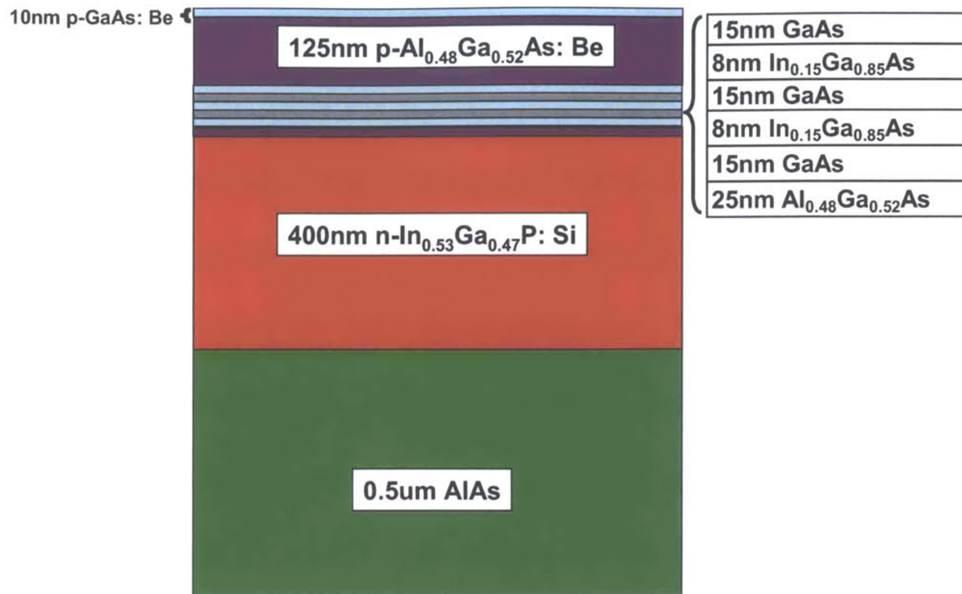

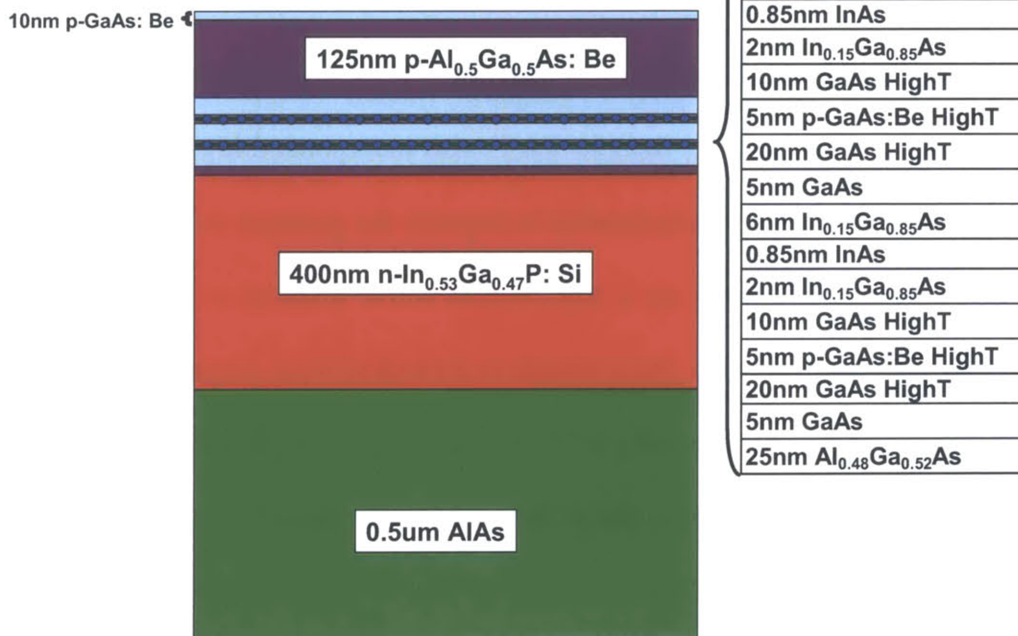

Figure 11: Schematics of the grown epiwafers.

Since different gain regions have different advantages, several were grown. Quantum dots are formed by the growth of highly lattice-mismatched InAs on GaAs or low In content InGaAs. Due to the lattice mismatch strain, the InAs forms small islands

of material during the first few monolayers of growth. The overgrown InAs islands confine carriers in three-dimensions causing the carriers to occupy very specific electronic states (much like a microcavity). The number of electronic state possibilities for a given energy per unit crystal volume is given by the density of states function, $\rho(E)$. The discrete density of states caused by carrier confinement in quantum dots is expected to produce a very narrowband emission spectrum, allowing greater Purcell enhancement as mentioned in Chapter 2. The discrete density of states also means that the injected carriers quickly thermallize to energy levels that are resonant with the cavity photons. The high differential gain, dg/dN of quantum dots decreases the turn-on time of the semiconductor lasers. Both samples VA28 and VA35 were grown with quantum dots buried inside an InGaAs quantum well. However, sample VA35 was grown so that the InAs quantum dot layer was sandwiched between two InGaAs layers as opposed to being grown on top of a GaAs layer. Sample VA35 also incorporated high temperature GaAs spacer layers and Be-doped GaAs barriers to improve the quantum dot quality [29].

Strained quantum wells are a well-studied active material with many advantages over unstrained quantum wells. Most notable is the reduction in Auger recombination due to an increased valence band curvature [7]. The strained quantum well in sample VA34 is an 8 nm thick $In_{0.15}Ga_{0.85}As$ layer surrounded by GaAs barriers. Although sample VA34 was designed to ideally emit light at 980nm, a wavelength that is not applicable to integrated optics, sample VA34 was incorporated into one of the microcavity laser designs to prove the concept of the microcavity laser.

The photoluminescence (PL) spectra for all of the structures are shown in Figure 12. The PL spectrum is measured by exciting a sample with a laser emitting photons with

an energy above the bandgap energy and by observing the emitted light from the sample due to spontaneous decay. The PL spectrum shows the emission behavior of the sample without the effects of the laser microcavity. From the figure, the strained 8 nm thick $In_{0.15}Ga_{0.85}As$ quantum wells (sample VA34) are observed to have the narrowest emission spectrum and emitted at 960nm. The 980nm emission peak in sample VA28 is due to the InGaAs quantum well covering the InAs quantum dots. The emission peaks from the quantum dot layers occurred at ~1050nm in sample VA28 and ~1245nm in sample VA35. The broad emission spectrums of samples VA28 and VA35 is due to the spread in quantum dot sizes which leads to a broader density of states and thus a broader emission spectrum. For this reason, experiments in the strong coupling regime usually utilize as few quantum dots as possible.

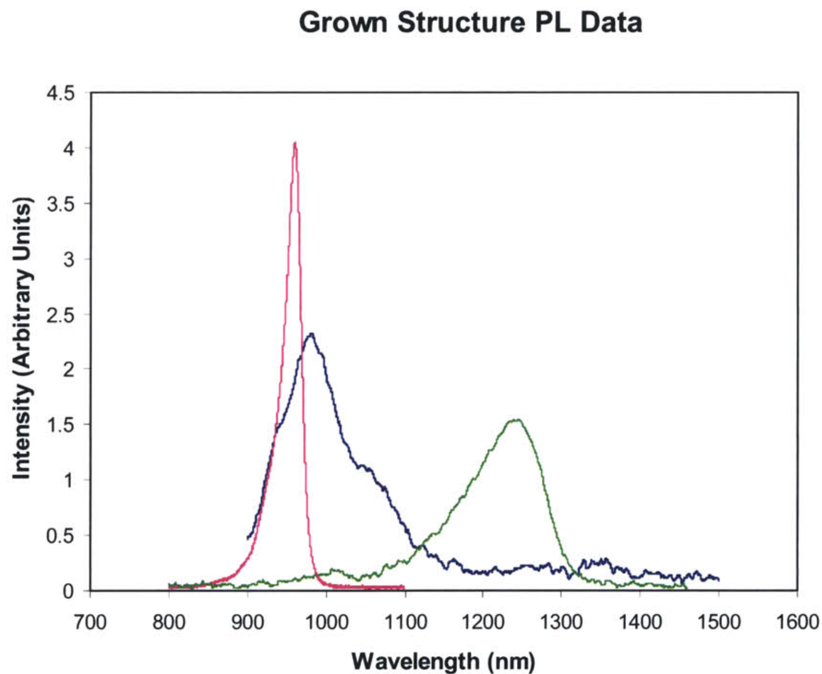

Figure 12: Photoluminescence data for grown epilayers

3.2.1. Optical Simulations

Design software from *Optiwave* was used to ensure a proper modal overlap between the various sections of the lasers and the optical mode. The program uses the beam propagation method (BPM) to calculate the electromagnetic field behavior as light traverses a device. The *Optiwave* BPM software assumes paraxial rays and does not take backward reflections into account. A detailed explanation of BPM can be found in [30]. Using a cross-section of the microcavity laser, the transverse electric field distribution of the guided mode was analyzed

The index of refraction of most of the materials was taken from [31]. If the index was not given for a particular alloy, a superposition of the index of refraction of known alloys was used. The index of AlGaAs was found by using a numerical equation found in [32]. The code that was used to determine the index of refraction of AlGaAs is found in Appendix 1. The index of refraction of all layers was assumed to be constant with carrier density. Each device width was set to 600nm as this width resulted in a waveguide with single guided mode. Figure 13 shows the simulated horizontal component of the guided electric field for each structure. Since the electric field is perpendicular to the direction of propagation, this is referred to as the Transverse Electric (TE) polarized mode. As seen from the guided modes, the fundamental mode overlaps both the gain material and the output waveguide in all cases.

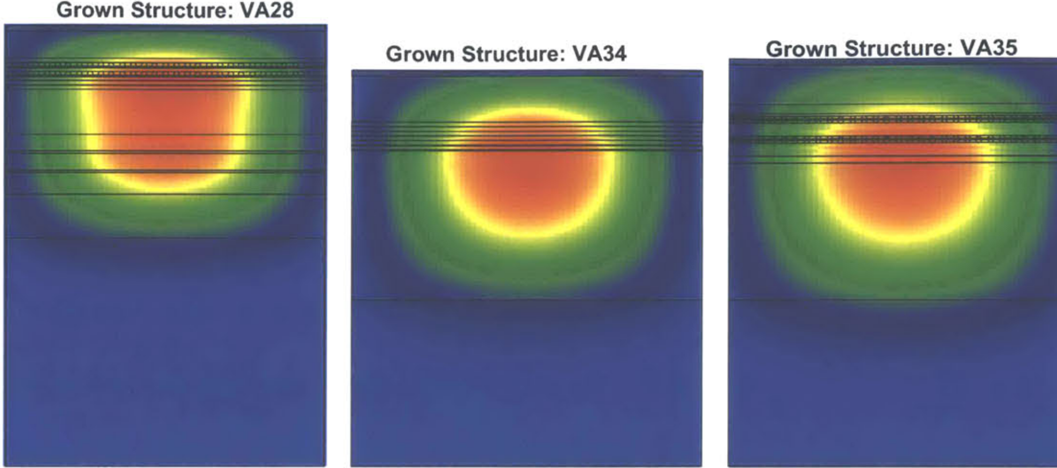

Figure 13: Grown structures and their transverse fundamental mode distributions.

3.3. Rate Equation Calculations

One goal of this thesis was to theoretically predict the behavior and relevant figures of merit for the laser herein. The phenomenological rate equation model found in [7] is used. The rate equations for the carrier concentration and photon density can be written as:

$$\frac{dN}{dt} = \eta_i \frac{I}{qV} - CN^3 - BN^2 - A_d N - A_{surf} N - v_g \frac{V_p}{V} \Gamma g N_p \tag{5}$$

$$\frac{dN_p}{dt} = v_g \Gamma g N_p + \frac{V}{V_p} \beta_{sp} B N^2 - v_g < \alpha > N_p \tag{6}$$

where N is the free carrier density in the active region (cm^{-3}), and N_p is the lasing mode photon density in the laser cavity (cm^{-3}). The physics behind each term as well as the values for each constant are given in Appendix 2. The term, $\frac{V_p}{V}\Gamma$, that is present in the carrier rate equation is different than in reference [7] and most other texts because V_p is defined as the physical photon cavity volume rather than the modal volume as in other books. The factor V_p/V accounts for the fact that photons occupy a greater volume than

the active material and the factor, Γ, accounts for the non-uniform energy density distribution that photons must satisfy in a cavity. This notation is used to stress that if there is no modal overlap with the active region (Γ=0), then there can be no stimulated emission. This term is not present in the spontaneous emission term, because even if the lasing mode does not overlap the active region, other vacuum modes can still cause spontaneous emission.

Since, the time dynamics of the laser are not being analyzed, the laser is assumed to be in steady state meaning that the time derivatives in the above rate equations are zero. When equation (6) equals to zero, the density of lasing-mode photons in the cavity is given by the following equation [33].

$$N_p = \frac{\frac{V}{V_p}\beta_{sp} B N^2}{v_g < \alpha > - v_g \Gamma g} \tag{7}$$

Equation (7) is the driving equation for laser action. Physically, it shows that there are two processes responsible for laser action: Stimulated emission in the denominator, and spontaneous emission in the numerator. The denominator contains the loss minus the gain due to stimulated emission in the lasing mode. The gain can *never* equal the loss otherwise the photon density will be infinite [33]. In fact, as the gain *asymptotically* approaches the loss, the photon density in the lasing mode increases and laser action is observed. This is in contrast to the normal method of defining threshold as the point where gain equals loss, a case which can not exist.

The numerator in equation (7) is the spontaneous emission rate into the lasing mode. For conventional lasers where β_{sp} is small, the numerator is very close to zero, and the gain can be very close to the loss without introducing any singularities. In

microcavity lasers, β_{sp} can be quite large meaning that spontaneous emission can also drive laser action. Moreover, in microcavities, the gain can be much smaller than the loss and N_p can still be large enough for linewidth narrowing to be observed– the hallmark of laser action. If β_{sp} is large enough, the material gain, g, can be less than zero (no population inversion), and there can still be a substantial amount of photons present in the lasing mode! Hence, the phrase "Lasing without population inversion." [34]. This can be physically understood by recognizing that even though the medium is absorbing photons (since the gain is less than zero), there is a good probability of re-emitting the photons into the lasing mode. Consequently, no measured loss of lasing-mode photons is observed [13]. Usually laser action is characterized by a dramatic change in efficiency at threshold once stimulated emission becomes dominate. For high β_{sp}, the numerator plays a larger role and the change in efficiency is less or not noticeable at all as in the case of a thresholdless laser.

The photon modal loss (cm^{-1}) can be separated into two loss terms acting simultaneously: the internal loss, and light lost from the photonic crystal mirrors, some of which is useful.

$$< \alpha > \ = \ < \alpha_i > \ + \ < \alpha_m > \tag{8}$$

The output power is given by,

$$P_{out} = F\, v_g < \alpha_m > h\, f\, N_p\, V_p \tag{9}$$

where F is the proportion of photons exiting the output photonic crystal mirror as compared to the opposite mirror. Multiplication by the photon volume converts the photon density lost due to the mirrors per unit time to the actual number of photons being emitted per unit time. Note that equation (9) explicitly illustrates the direct dependence of the output power on the cavity volume. In general, the larger the cavity, the more photons

the cavity can store, and thus the more photons that the cavity is capable of emitting per unit time. So while microcavity lasers might have many benefits, they will not be useful for any high power applications, unless an array of lasers is used.

Since data was readily available, the material parameters for strained quantum wells were used for all material dependant values in the simulations [7]. A wavelength of 960nm, corresponding to the emission peak of the grown strained quantum wells sample, was assumed. Because the *Optiwave* software package can not calculate the confinement factor, it was set to V/V_p. Future modal calculations should use a program that can calculate the confinement factor, so that more accurate results can be obtained. If the gain is assumed independent of polarization, the confinement factor is simply the photon energy in the gain material divided by the photon energy in the entire cavity.

Although β_{sp} is the most important factor for microcavities, it is also the most difficult to calculate. Several groups have calculated β_{sp} for different cavities, but the calculations are quite involved [35,36,37,38]. Thus, the spontaneous emission factor is parameterized in the calculations. A spontaneous emission factor of 0.01 is expected from measurements on micropost VCSELS [39], which are similar to this laser in terms of light confinement. Nonetheless, β_{sp} is varied from 0.005, a worst case scenario calculated by Erchak [40], to 0.05, a best case scenario measured in [26].

Using methods, which are further explained in Appendix 2, light (power) versus input current (L-I) curves were calculated. Figure 14 illustrates the results and shows that the output power is predicted to be small - on the order of micro-amps. This does not include coupling losses from the laser into the output waveguide, or propagation losses as the light propagates through the waveguide. Detecting the light will be difficult with a

fiber connected to a detector. For this reason, lasers integrated with photodetectors were added to the mask design, so that light could be detected without worrying about extra coupling losses.

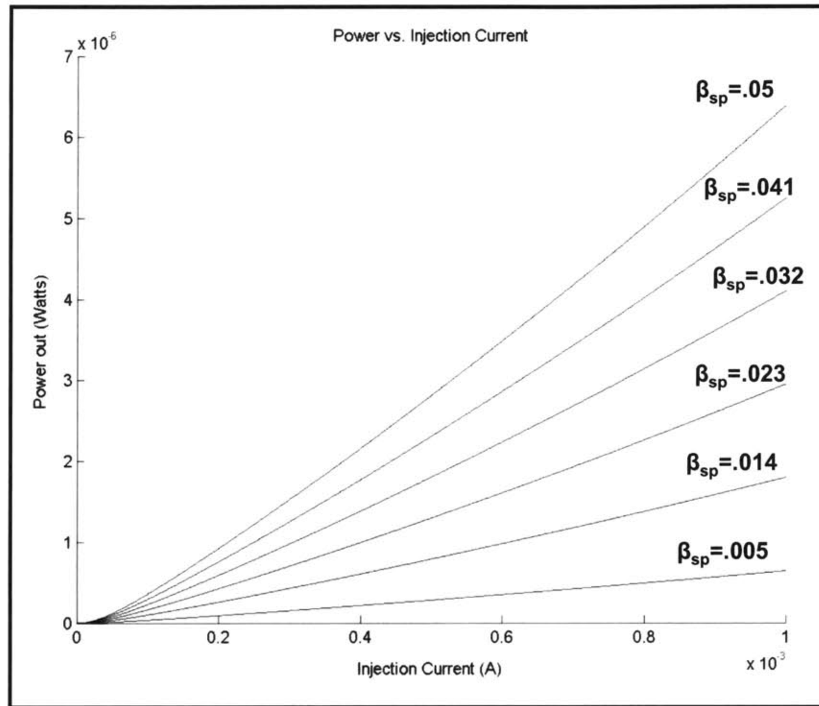

Figure 14: L-I curves for the photonic crystal microcavity laser.

In microcavity lasers, the conventional way of defining threshold as the point where gain equals loss is no longer valid. It can be shown, from Einstein's treatment, that the spontaneous emission rate into the lasing mode equals the stimulated emission rate when there is one photon in the lasing mode [41]. Since threshold is the point where stimulated emission begins to dominate spontaneous emission (this occurs when linewidth narrowing is observed), threshold can be rigorously defined as the point where there is one photon in the cavity [42]. Only when N_pV_p=1, a photon survives long enough

to induce other stimulated emission events. Using this definition, the threshold injection currents for the above six cases were determined and are shown in Table 1.

β_{sp}	0.005	0.014	0.023	0.032	0.041	0.05
$\eta_i I_{th}$ (μA)	446	193	133	106	89	79

Table 1: Calculated threshold injection currents for the photonic crystal microcavity laser.

The calculated threshold injection currents are in good agreement with the 300μA terminal current observed in [26] and the 260μA terminal current observed in [25]. For a reasonable injection efficiency η_i, and a reasonable spontaneous emission factor, β_{sp}, the proposed microcavity laser could yield the smallest threshold current for an electrically-activated photonic crystal laser to date. The laser will undoubtedly yield the smallest threshold current for an electrically-activated edge emitting laser.

3.4. Mask Design

In total, nine masks are required to fabricate the photonic crystal microcavity laser. In Chapter 4, a fabrication sequence is presented which incorporates only a single electron-beam lithography step. Because photolithography is used in lieu of electron-beam lithography in the fabrication sequence, a large burden rests on the proper design of the optical masks.

Great care was taken to design a mask set that simplifies both fabrication, and testing. A step and repeat design is used so that many lasers with varying dimensions can be fabricated at once. A die measuring ¼"x ¼" contains 208 lasers each with varying features allowing one to empirically determine the optimal laser. To facilitate electron-beam lithography, arrays of 6 lasers are fabricated within a 200μm x 200μm electron-beam field, the area the electron beam can access without moving the sample stage. This

also simplifies testing, because a fiber connected to a detector will only need to be displaced by more than 35μm after every 6th laser. In addition, arrays of lasers have practical applications in telecommunications. The output waveguides are angled by 7° relative to the cleavage plane to prevent reflections from the output facet. The contacts are distributed so that only one probe needs to be moved after testing each laser. Many diagnostics are included and are shown in Figure 15. Some of the more important diagnostics are described in the section that follows.

A.)

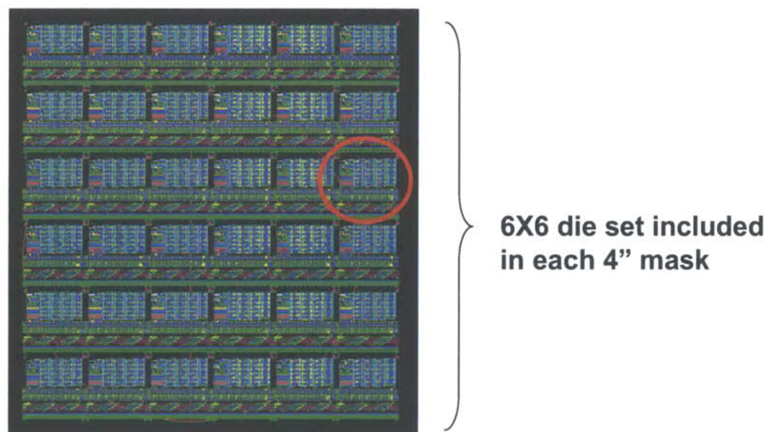

B.)

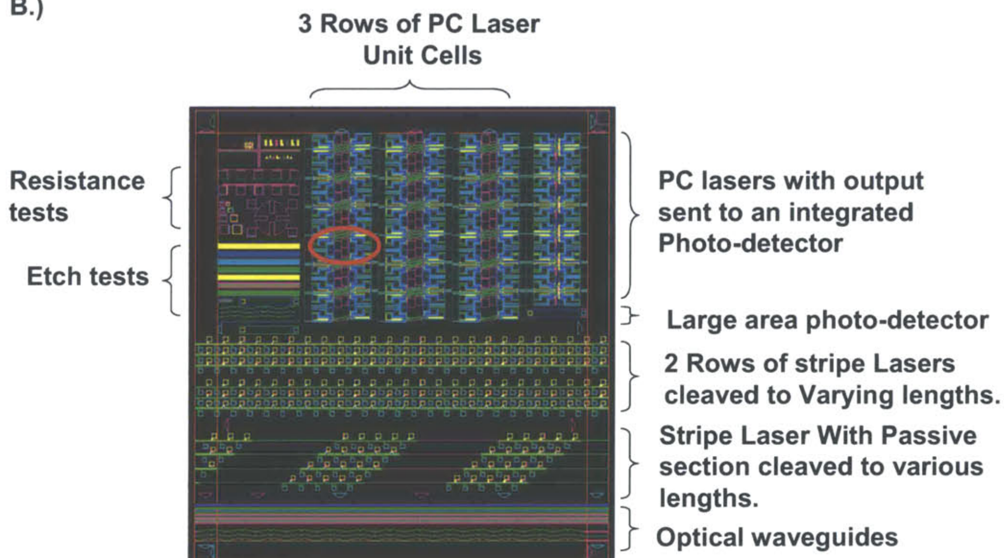

C.) Unit Cell

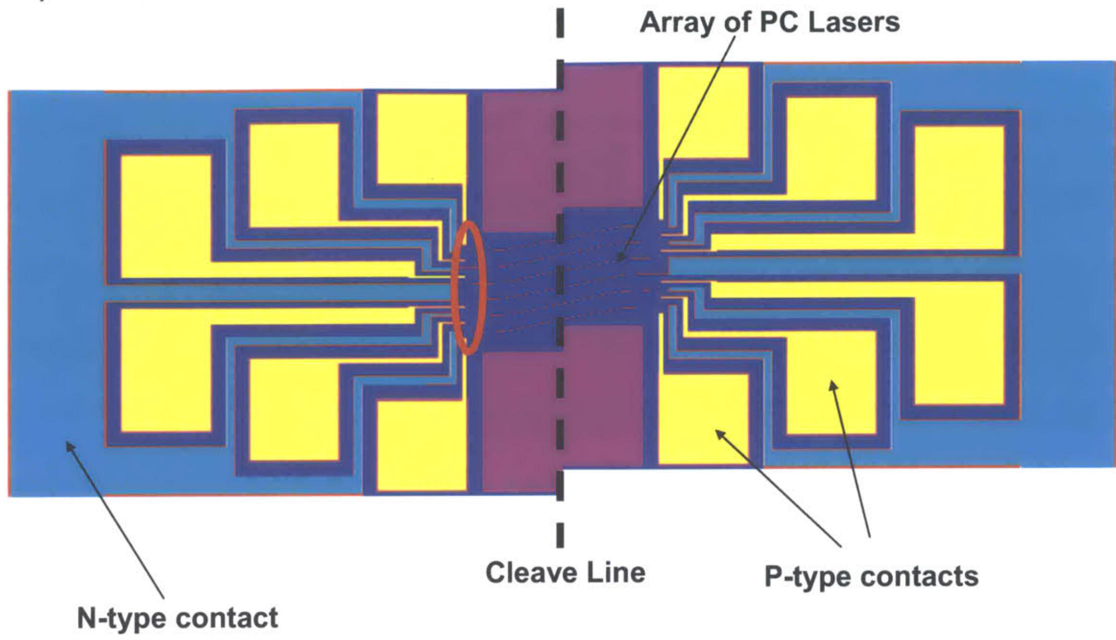

D.) Laser Array

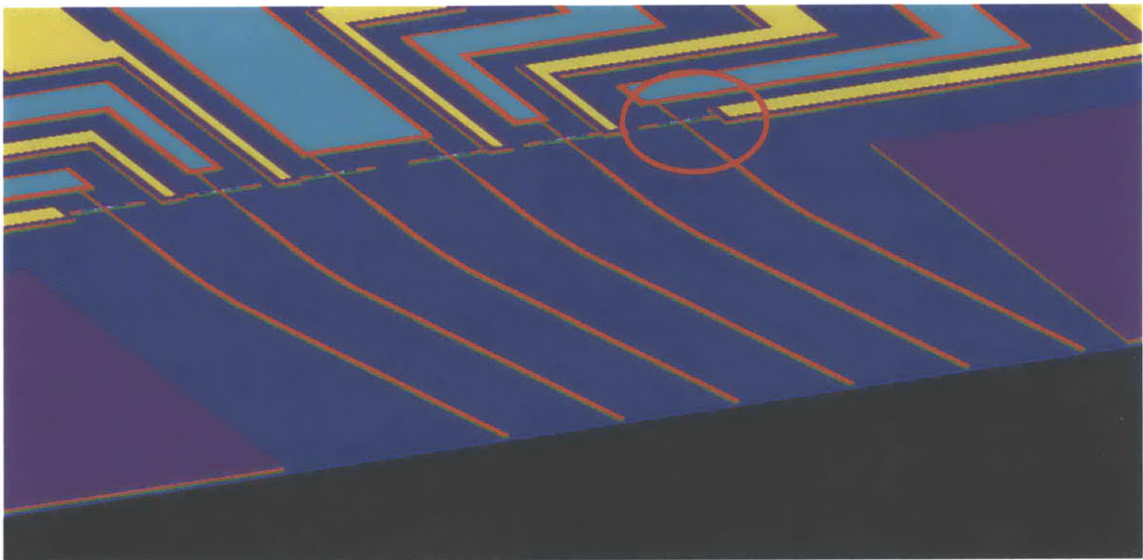

E.)

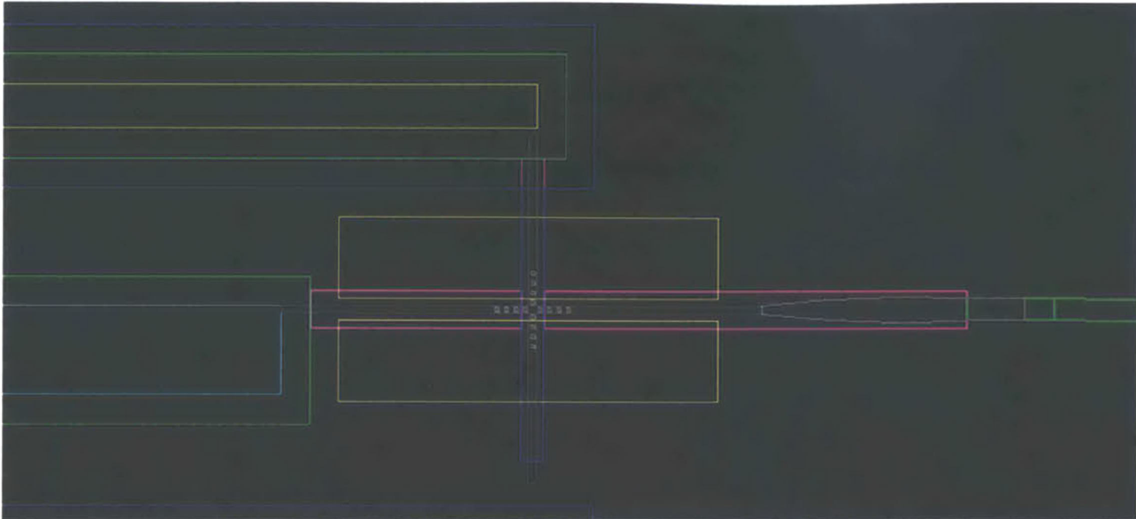

Figure 15: Mask views with varying zoom levels. The red ovals indicate the region shown in the subsequent zoom level. A.) The entire step and repeat mask includes 36 identical dies, B.) Each die consists of 234 lasers of varying dimensions and many diagnostics. C.) Each unit cell on the die contains 12 lasers and accompanying contacts. D) An array of 6 lasers each separated by 30μm. E.)Each laser requires 8 masks to fabricate.

3.4.1. **Stripe Laser Diagnostic**

One advantage of optical lithography is the easy incorporation of diagnostic devices without additional fabrication effort. While the incorporation of diagnostic devices complicates the optical mask design, their utility should warrant the extra time spent during the design phase.

One such diagnostic device is a stripe laser which is used to test the quality of the lasing material and serves as an important verification of the design before commencing the timely electron-beam lithography step. The stripe lasers consist of six rows of stripes that can be cleaved to various lengths to form cleaved facet lasers. The lasers are simple stripe-loaded waveguide structures with contacts for carrier injection. The stripe ridge can be viewed as a region with a large effective index within a slab waveguide and thus confines the fundamental mode to areas directly below the ridge. Ridge widths of 2, 4,

and 6μm are included on the mask. A schematic of a single stripe laser is shown in Figure 16. The upper *p*-type material is colored purple while the lower *n*-type material is colored in red. The *p*-type contact is highlighted yellow; the lower *n*-type contact is highlighted in blue. Cleaved facets are used as mirrors. An undercut is also necessary to isolate the *p* and *n* type regions but unfortunately requires an extra fabrication step.

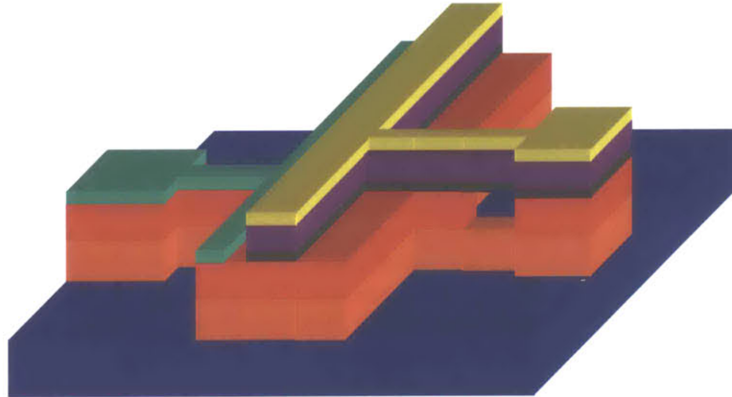

Figure 16: Schematic of a single stripe laser diagnostic device.

Also included in the mask design are stripe lasers integrated with a passive waveguide. By offsetting identical structures in the mask design, at least two stripe lasers with identical active lengths, yet non-identical passive lengths, will result after cleaving. By comparing the output characteristics of each laser one can then determine the loss in the passive section.

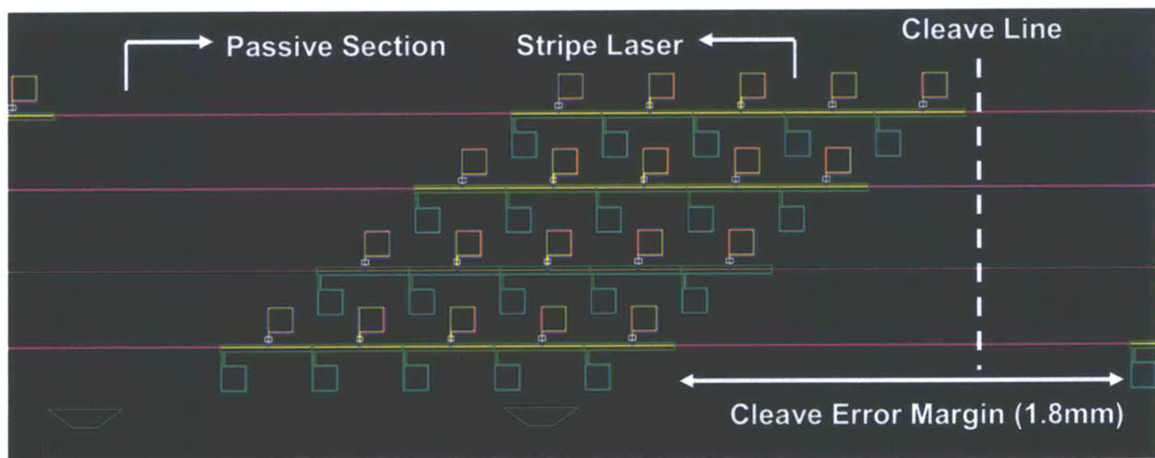

Figure 17: Mask layout of stripe laser with integrated passive section

3.4.2. **Integrated Diagnostic Detector**

Since the output power of the photonic crystal microcavity laser is predicted to be quite small, an integrated diagnostic detector was included in each of the mask dies. As seen in Figure 18, the detector appears much like the photonic crystal laser except that the holes are entirely removed from the input. However, holes are included on the opposite side, so that the detected light will reflect off the photonic crystal mirror effectively doubling the absorption length in order to increase the sensitivity of the detector. Also, the detector incorporates a wider upper *p*-type beam to increase the detector's absorption length. Finally, a slice of material is removed from the input side to electrically isolate the reverse biased detector from the forward biased laser. Since this slice is included in the electron beam mask, it can be placed anywhere between the detector and laser without modifying the optical photolithography masks. The total distance between the photonic crystal laser and the integrated detector is 100μm. In comparison to the stand-alone photonic crystal laser, the length of the output waveguide is 200μm.

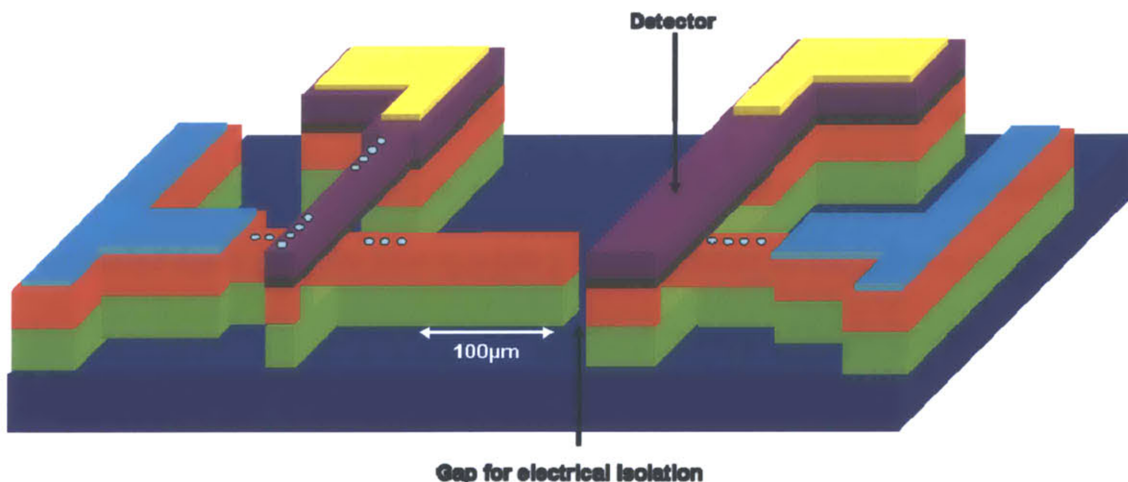

Figure 18: The integrated diagnostic photodetector

Chapter 4.

Fabrication

4.1. Fabrication Sequence

Due the complicated nature and time required for electron-beam lithography, the aim of the fabrication sequence is to pattern all of the small features with a single electron-beam lithography step and to reduce the time required for the electron-beam lithography step. The first criterion is accomplished by using conventional, contact photolithography to pattern all of the large features such as the electrical contacts, and by using electron-beam lithography to only trim the large features. The second criterion is met by placing 6 lasers within a single electron-beam lithography field, and again by using electron-beam lithography only for small features. Consequently, most of the fabrication sequence uses standard photolithography. While the proposed hybrid lithography scheme increases the time spent during the design phase because more processing steps are required, it allows for a process flow consisting of mostly simple photolithography and etch steps. Finally, due to the use of contact lithography, all the features across a wafer can be patterned during one exposure allowing many variations of the laser to be incorporated easily onto a single wafer.

Figure 19 summarizes the fabrication sequence. Standard photolithography and lift-off processes are used to define the electrical contacts. Depositing the contacts on a bare substrate leads to better ohmic contacts, since fabrication damage to the surface is

minimized prior to the deposition of the ohmic contact metal. Depositing the metal first also creates highly visible base alignment marks. Previous work [43] revealed that alignment to previously defined features became difficult during subsequent electron-beam lithography steps due to the absence of metal alignment marks. Furthermore, metal base alignment marks allow one to consistently align each mask to the same feature eliminating the deviations that often accompanies alignment to progressively defined and created features.

A series of photolithography steps and III-V material etches are used to define the contact mesa, the upper *p*-type cross beam and the *n*-type lower passive waveguide. A hybrid electron-beam lithography and photolithography approach is used to define the submicron features of the photonic crystals and the microcavity. Finally, via openings through a protective dielectric layer, an undercut of the upper waveguide and an AlAs oxidation process step are performed. In general, entire two inch GaAs wafers were fabricated. Within the process flow, diagnostic stripe lasers can be created and tested to ensure that the gain medium is capable of emitting at the desired wavelength.

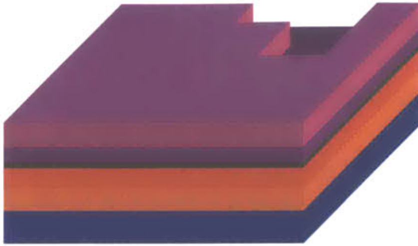
1.) Deposit and Pattern Photo resist

2.) Apply and Lift-off P-type metal

3.) Pattern Resist to Define P-type beam

4.) Wet Etch to Phosphide Remove Resist

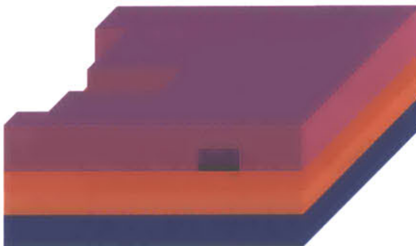
5.) Pattern Resist For N-type Metal

6.) Apply and Lift-off N-Metal

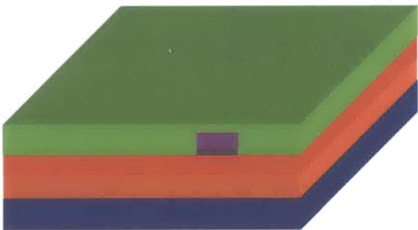
7.) Deposit PECVD oxide

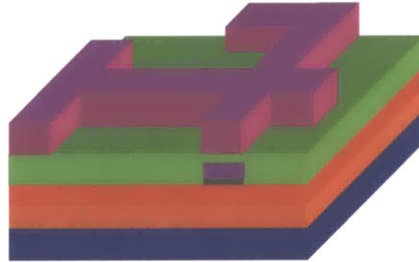
8.) Apply and Pattern Photo resist

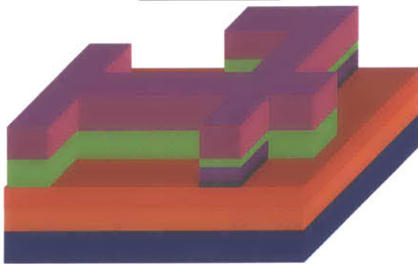
9.) Etch Oxide

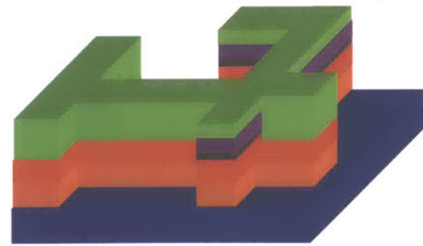
10.) Remove Resist Dry etch to substrate
Undercut and test Stripe Lasers

11.) After a combination of E-beam and optical lithography

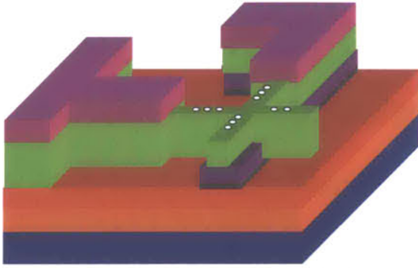

12.) Perform 3 RIE etches to substrate

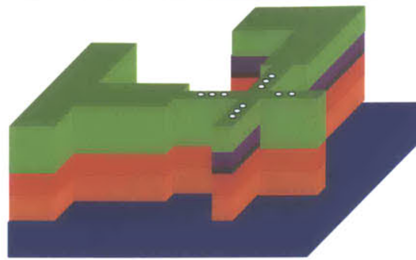

13.) Apply and Pattern Resist for undercut

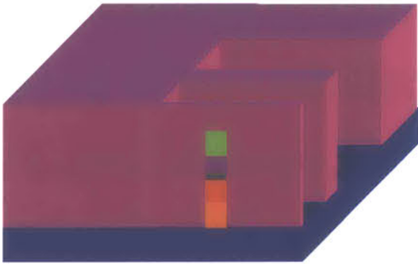

14.) Undercut and Remove Resist

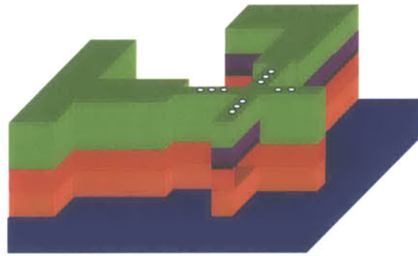

15.) Open up vias to Contacts

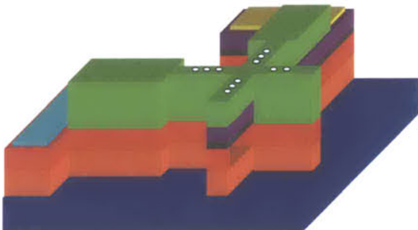

16.) Oxidize bottom AlGaAs then test

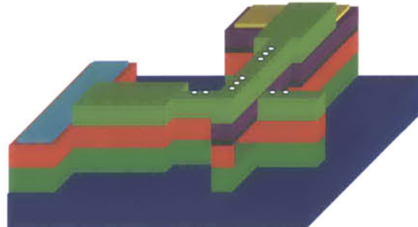

Figure 19: Fabrication sequence for the electrically-activated microcavity laser and the diagnostic stripe laser. Steps 8-10 are only required to fabricate the diagnostic stripe lasers before electron beam lithography, or focused ion beam etching.

4.2. Fabrication Results

4.2.1. Steps 1-2: Formation of ohmic contacts on p-type arsenide-based material

A good ohmic contact is critical to obtain a low-power laser. A contact with a large contact resistance can be viewed as a resistor in series with the diode laser. Although the contact resistance does not affect the threshold current, it does affect the voltage required to reach I_{th} and thus the input power. In addition, the power dissipated across the ohmic contact heats the laser which degrades the optical performance of the laser.

Whenever a metal and a semiconductor come into contact, the Fermi-levels in the semiconductor and in the metal align so that an equilibrium is reached. The difference in the free charge and the electron affinity between the metal and the semiconductor, results in a built-in electric field and thus a potential barrier (much like a *p-n* junction) [44]. A good ohmic contact occurs when the tunneling current is much larger than the thermionic emission current over the built-in potential barrier. The band alignment between a metal and a semiconductor, along with the associated potential barrier, Φ_B, is shown in Figure 20. Low resistive ohmic contacts are achieved by heavily doping the semiconductor at the interface to reduce the width of the barrier and by choosing a metal with an electron affinity close to that of the semiconductor to reduce the height of the potential barrier [45]. Since tunneling is a linear process, an ohmic contact results in a linear I-V characteristic.

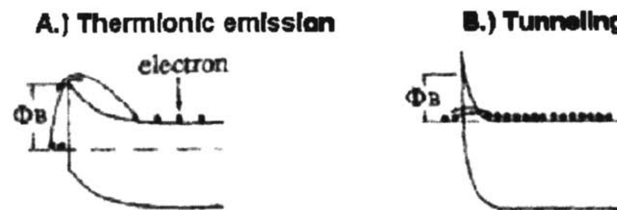

Figure 20: A) The band diagram and potential barrier associated with thermionic emission. B) The band diagram and potential barrier associated with carrier tunneling.

Several metals were considered to make an ohmic contact to a 10nm thick, heavily doped contact layer of GaAs:Be with a 125nm thick AlGaAs:Be cladding layer underneath. The Au/Mn/Ni/Au structure has been found to have an extremely low contact resistivity of $1.6x10^{-8}\Omega\ cm^2$ [46], but Mn is not available in the NanoStructures Laboratory (NSL). Another contact that exhibits good adhesion and excellent surface morphology due to the absence of Au is based on the Ni/Zn/Al system [47]. However, a

self-aligned contact is used for the diagnostic stripe lasers, resulting in the ohmic contact metal being left unprotected by photoresist during the etching of the arsenide-based material. Since AlGaAs is etched, an Al-containing contact might not withstand the wet-etch. In light of these limitations, the Au/Zn/Au multilayer structure was chosen. The Au/Zn/Au structure has been shown to have a contact resistance of $3 \times 10^{-6} \Omega$ cm^2 and to have good adhesion to p-GaAs [48]. Since the thickness of the epilayers was a concern for sample VA28, a Au(300Å)/Zn(370Å)/Au(830Å) ohmic contact metallization scheme was used. Subsequent samples utilized a contact structure consisting of Au(300Å)/Zn(370Å)/Au(2000Å) as recommended in [48].

A lift-off process was used to pattern the *p*-type ohmic contacts. Clariant AZ5214 image reversal photoresist was used in step 1. Image reversal photoresists are used in lift-off processes because these photoresists provide inward-slanted sidewalls, which allow solvents to penetrate between the metal layers and the photoresist during the lift-off process. The most reliable photolithography process in the Technology Research Laboratory (TRL) for lift-off processes is outlined below.

AZ5214 photoresist image reverse process

Solvent Clean: Acetone, Methanol, Iso-propanol
HMDS 30 minutes: Recipe 5 in TRL
Allow wafer to cool for 3 minutes
Coat Wafers:
- Dispense: 500rpm, 6 seconds
- Spread: 750rpm, 6 seconds
- Spin: 4000rpm, 30 seconds

Prebake: convection oven at 95° for 30 minutes
Expose using EV1 contact aligner for 1.5 seconds
- Alignment Seperatation: 30μm
- Contact Mode: Hard Contact
- Mask Thickness: 1.6mm
- Substrate Thickness: 352μm

Reversal Bake: convection oven at 95° for 30 minutes
Flood Expose on EV1 for 60 seconds
Develop in AZ422 developer for ~100 seconds

Prior to metallization, all of the samples were descummed in NSL to remove any residual resist from step one. The descum process consists of a plasma of helium and oxygen which removes any organics such as photoresist from the surface. Details of the descum process are listed below. Following the descum process, the ohmic contact metals were evaporated onto the samples using the NSL electron beam evaporator. Due to the high vapor pressure of Zn, the system pressure was kept at, or below 2×10^{-6} Torr during the metal deposition [48].

Descum process in NSL Plasmatherm

First clean the chamber for 4 min. using a CF_4/O_2 Plasma

Descum sample in He/O_2 Plasma

- Chamber Pressure: 7mtorr
- He flow rate: 5sccm
- O_2 flow rate: 10sccm
- Power: 150W
- Time: 20 sec after plasma sparks

After metallization, lift-off was performed in NSL using a hot N-methyl pyrimidinone (NMP) process. After heating the NMP to 130°C using a hot plate, each sample was placed in the solution and gently stirred for a duration lasting between 15-30 minutes. The process consistently removed the unwanted metal and photoresist on each sample. Examples of metal features are shown in Figure 21. As will be mentioned later, alternative alignment marks should be included for better precision.

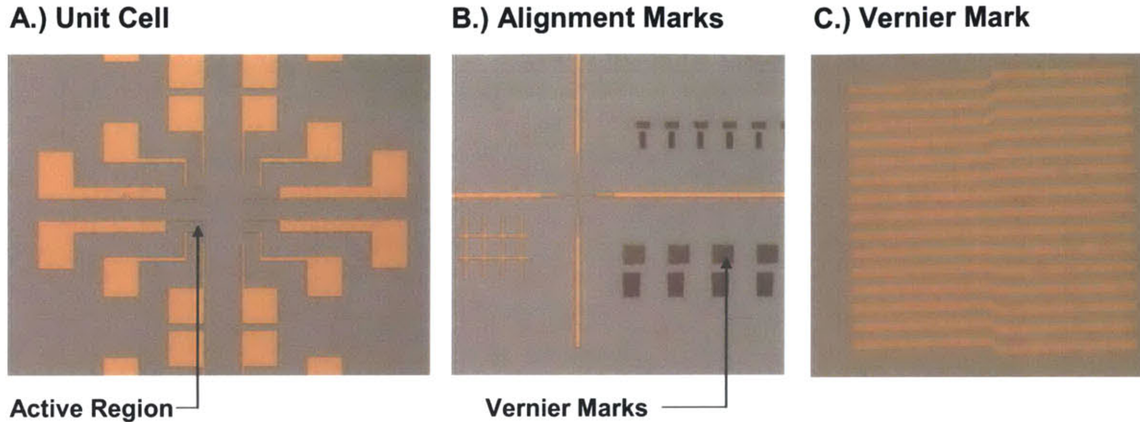

Figure 21: Metal features after steps 1-2. A) A unit cell containing 6 active regions. B) Alignment marks C) Vernier alignment marks as viewed with a 50X objective. Each line is 1.5μm wide with a minimum spacing of 1.5μm between each line.

4.2.2. Steps 3-4: Wet-etching of Arsenide based material

The purpose of steps three and four is to pattern and etch the upper arsenide-based material. The arsenide-based material in the active regions will eventually be trimmed during the electron-beam lithography and subsequent etching process steps. Removing the upper arsenside-based material allows the electrical contacts to the bottom phosphide-based material to be created. The ridge of the stripe diagnostic laser is also formed during the etching of the arsenide-based material with the *p*-type ohmic contact metal serving as a self-aligned etch mask.

The resist pattern in step 3 was formed by using Clariant AZ5214 photoresist as a positive resist. The positive AZ5214 resist process produces sidewalls with lower roughness than the Arch Chemical OCG 825 photoresist; the more commonly used positive resist in TRL. Smooth sidewalls are necessary for acceptable stripe lasers. The details of the AZ5214 positive resist process is listed below. After patterning, the wafers were descummed using the same process that was described in step 2, except the plasma was terminated 10 seconds after the plasma ignition. By removing just a very thin layer of resist, the descum process decreases the photoresist sidewall roughness.

AZ5214 photoresist positive process

Solvent Clean: Acetone, Methanol, Iso-propanol
HMDS 30 minutes: Recipe 5 in TRL
Allow wafer to cool for 3 minutes
Coat Wafers:
  Dispense: 500rpm, 6 seconds
  Spread: 750rpm, 6 seconds
  Spin: 4000rpm, 30 seconds
Prebake: convection oven at 95° for 30 minutes
Expose using EV1 contact aligner for 10 seconds
  Alignment Seperatation: 30µm
  Contact Mode: Hard Contact
  Mask Thickness: 1.6mm
  Substrate Thickness: 352µm
Develop in AZ422 developer for ~100 seconds
Vacuum cure: 15 min. 10^{-5} torr

Following resist patterning, the arsenide-based material was etched in a solution of 1:1:10, H_2SO_4:H_2O_2:H_2O [49]. The reaction was fast and uncontrollable with features even 10µm in width being completely undercut. Although 10µm features were being undercut, the sulfuric acid/hydrogen peroxide-based solution preferentially etches arsenides as opposed to phosphides so that the etch depth equals the total thickness of the arsenside-based layers which is sample dependent. In an attempt to minimize the undercutting, the solution was diluted with deionized water and its temperature was controlled through the use of a room temperature water bath [50]. The water bath removes the heat that is generated from the exothermic reaction that occurs when sulfuric acid and hydrogen peroxide are diluted with water. Upon mixing the chemicals, approximately 20min is required for the solution and the water bath to reach the same temperature of 25±2°C. A final concentration of 1:1:40 H_2SO_4:H_2O_2:H_2O resulted in an etch rate of ~26Å/sec as measured by dipping a cleaved test wafer into the solution for 10 seconds per dip and then by measuring the resulting etch depth using a surface

profilometer. A general observation was that identical measurements could vary by about 200Å, so several features were measured to determine an average etch rate.

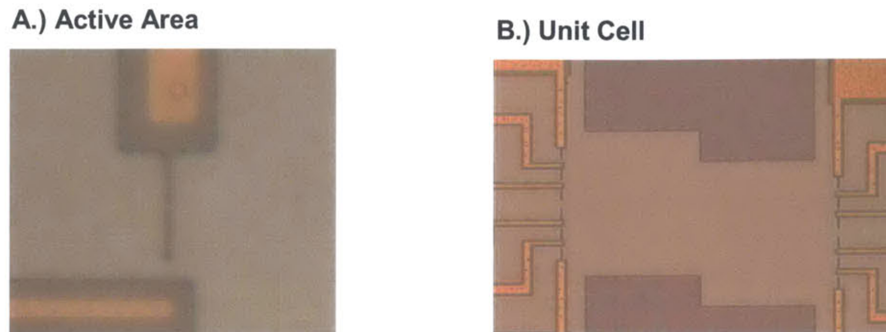

Figure 22: Photonic crystal laser features after removing the *p*-type material. A.) The active area of a laser with the patterned *p*-type beam defined. B.) A unit cell depicting a total of what will be 12 lasers. Compare to figure 15 (c).

4.2.3. **Problems with Metal Adhesion**

Although a usable wet-etch process was developed for the photonic crystal lasers, some critical problems with metal adhesion were revealed during this step. In particular, the metal on the alignment marks and stripe laser ridge were removed during the wet etch. Unfortunately, both of these features were left unprotected by photoresist in the mask design and hence experienced a partial undercut during the isotropic wet etch. Fortunately, some of the alignment marks and ridges survived, but not enough for a quality process. Figure 23 illustrates some of the features that were affected by the metal adhesion problem.

Initially it was thought that annealing the contacts might promote adhesion to the surface. Annealing causes the metal and semiconductor to intermix forming new compounds, which might promote adhesion. A 30 second rapid thermal anneal at 400˚C was performed before the wet-etch. This had little to no affect on the adhesion, but an anneal was performed on all subsequent wafers to be safe. After annealing, the metal surface became noticeably bumpy. Surface roughness due to annealing is expected and is

a motivation for using non-alloyed contacts [45]. However, no straightforward non-alloyed contact could be found in the literature [45]. Also, Au containing contacts are known to exhibit a poor surface morphology [47]. To verify that the metal was not being etched, the ohmic contact metal was evaporated on a bare silicon wafer and dipped for a total of one minute in a 1:1:20 H_2SO_4:H_2O_2:H_2O solution. No measurable etching of the metal occurred.

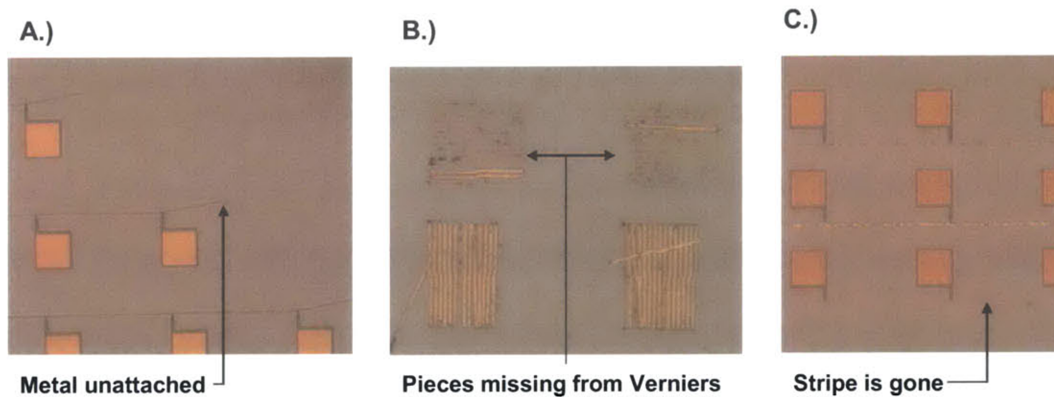

Figure 23: Examples of metal adhesion problems after wet-etch. A) Rows of stripe lasers with an integrated loss-section. Metal is only attached to the large contacts which were protected by photoresist. B) Vernier alignment marks have missing pieces. C) Three rows of stripe lasers with the 3rd row completely missing.

A scanning electron micrograph of the contact metal on a ridge of one of the lasers that was formed by wet-etching is shown in Figure 24. Immediately noticeable is the sloped, rough sidewalls of the ridge, and the uneven surface of the metal. Wet etches should yield smooth surfaces, but the semiconductor ridge is rough. Considering the magnification of the images, the sidewall roughness is estimated to be about 50nm, which is about 3% of the smallest stripe width. After annealing, the metal sidewalls might have roughened by a small amount. This roughness would then transfer into the underlying ridge. Consequently, an anneal should not be performed before the wet-etch although detailed studies were not carried out to confirm this hypothesis.

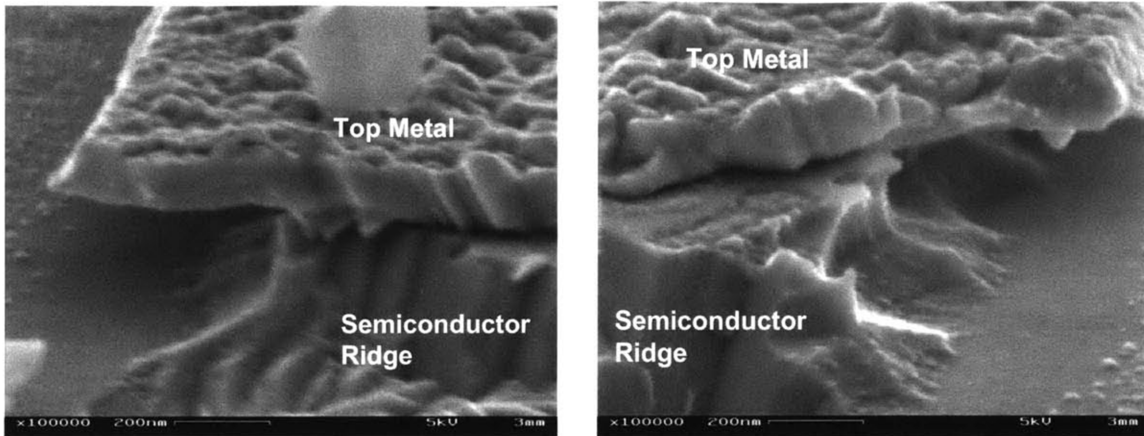

Figure 24: Annealed metal contact that was used to fabricate the self-aligned ridge waveguide. The lack of surface morphology is probably due to the contact anneal.

The features in Figure 24 also suggest one possible explanation for the metal adhesion problem. The undercutting process leaves about 0.2μm of overhanging metal on each side of the ridge. Since the smallest features are 1.5μm in width, there may not be enough material for the metal to adhere to after the etch. Another possibility is that a surface oxide develops on the GaAs before the metal is evaporated. A suitable process would then require a HF dip immediately prior to depositing the metal. One final possibility is that Au-based contacts simply do not adhere well to GaAs.

There are several options to alleviate the problems associated with the exposed metal during the wet-etching of the arsenide-based material. An immediate solution is to dry etch the wafers rather than wet-etch the wafers. Because a suitable dry-etch process can take a long time to develop, it was not attempted in this work, but once a process is developed, dry etching can be very effective. Since dry etching produces vertical sidewalls, there will be no overhanging metal. If indeed, the large amount of overhanging metal is the cause of the adhesion problem, dry etching would be an excellent solution, assuming the contact metal is also a good hard mask. Another option is to use a SiO_2 (or SiN_x) hard mask instead of the metal. This would entail the deposition of SiO_2 before step

1. Positive resist, rather than negative resist, would be patterned using the original metal mask, followed by etching the SiO_2. The SiO_2 hard mask would not be removed until the GaAs-based material is etched, after which the original *p*-type contacts are re-patterned onto the wafer using steps one and two [Figure 25]. This method does require good alignment during the re-deposition of the metal, but it avoids dry etching. Figure 25 illustrates how the ridge of a stripe laser would be formed using this method.

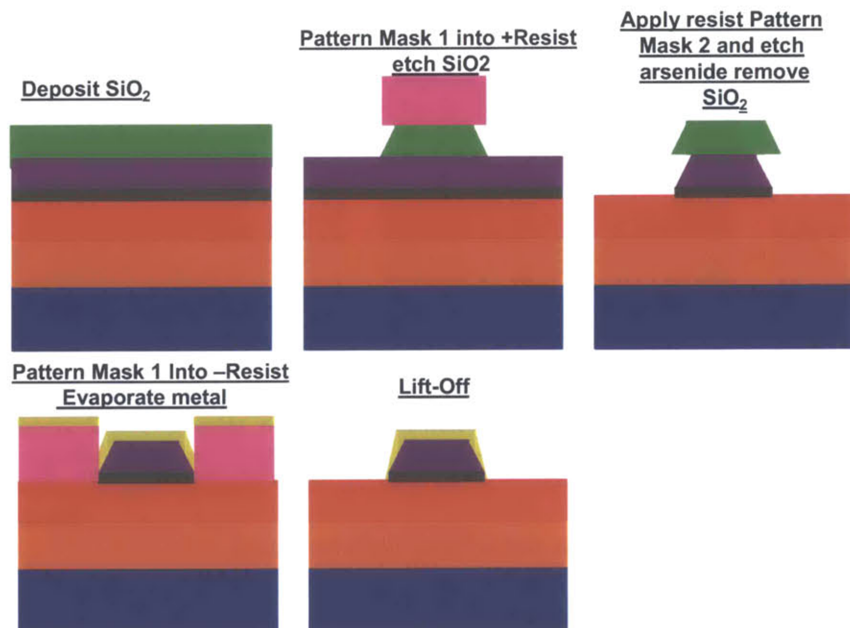

Figure 25: Cross-sectional schematics of an alternative method to form the ridge of the stripe laser without using metal as a wet-etch mask. This method does not require any dry-etching, but does require good alignment during the re-patterning of Mask 1. It is important to realize that one must apply and pattern Mask 2 before wet-etching the GaAs-based material in order to form the p-type beam of the photonic crystal lasers. Plus and minus signs in front of resist indicate positive or negative resist respectively.

Yet another option is to modify the existing mask set so that all of the metal features are protected by photoresist during the wet-etch. This entails a simple re-design of the base alignment marks and the integrated stripe lasers in mask 2. Of the three options so far, this would probably require the smallest amount of time, because no lab-related development is necessary.

Finally, one can simply continue the process as is, since there are a fair amount of stripe lasers and base alignment marks remaining on the wafer after the wet-etch. Unfortunately the stripe lasers with 1.5μm wide ridges usually do not survive the wet etch, but the stripe lasers with the wider ridges can still be used to test the material. Fortunately, a second set of electron-beam lithography alignment marks are formed during the patterning of the *n*-type ohmic contact metal [Figure 26], so that good alignment can still occur for each electron-beam field even in the worst case scenario where all of the base alignment marks no longer exist. Special care was taken in the mask design to protect the electron-beam lithography alignment marks during all subsequent steps. For negative photolithography processes, the alignment marks are already protected, but for the positive processes, a box was placed around the electron-beam lithography alignment marks to protect them from being etched. The use of a "cross within boxes" alignment marks makes it easy to obtain accurate alignments because the electron-beam written features do not cover the alignment marks. This is not the case for the global alignment marks that were created using mask 1. Thus, the electron-beam lithography alignment marks are recommended for any future mask designs.

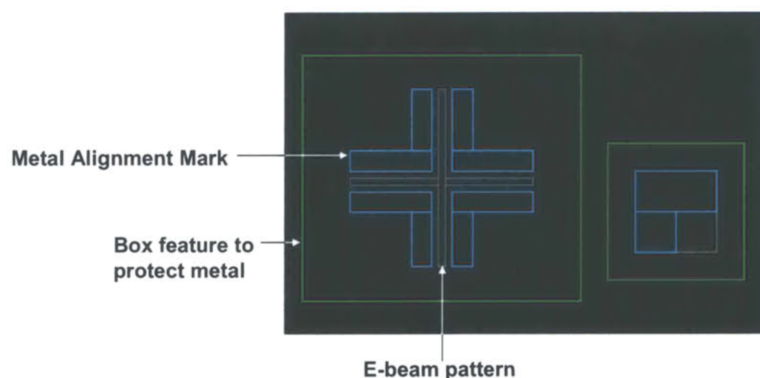

Figure 26: Electron-beam field alignment marks included in the mask design that were formed during second metal deposition.

4.2.4. Steps 4-5: Formation of ohmic contacts to *n*-type phosphide-based material

The most popular ohmic contact to *n*-type phosphide-based layers is AuGe/Ni/Au [51], but the AuGe alloy is not available in NSL. Therefore, a Au/Ge/Au contact, with a contact resistivity of approximately $10^{-7}\Omega cm^2$ was used [52]. The process used to form the *n*-type contacts is identical to steps 1-2 except that Au(400Å)/Ge(200Å)/Au(1600Å) was evaporated using electron-beam evaporation. Again, the photolithography and lift-off processes were very consistent resulting in well defined small features, such as the aforementioned electron-beam lithography alignment marks.

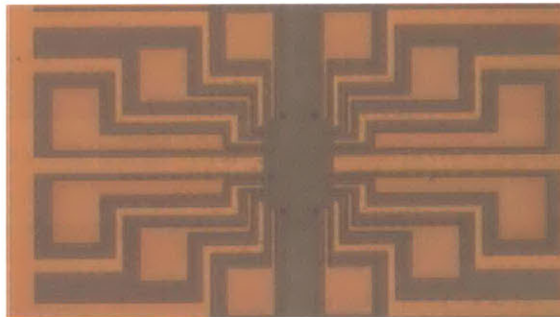

Figure 27: Unit Cell after steps 4-5. Compare to Figure 15(c).

4.3. Remaining Fabrication Steps: Discussion

Work on the photonic crystal laser was suspended after the second contact deposition. Consequently, some difficult fabrication steps still remain. Fortunately, past members of the Integrated Photonics Devices and Materials group have already undertaken many of these remaining processing steps. The aim of the following sections is to give suggestions on the remaining processing steps using the lessons already learned by these previous members, and to present the results from initial processing experiments that were performed as part of this thesis.

4.3.1. Steps 7-10: Dry etch of InP and GaAs materials. Patterning of SiO_2 hard mask

Steps 7-10 are only necessary to fabricate the stripe laser, or if Focused Ion Beam etching is used, to create the sub-micron features of the microcavity lasers. Since the stripe laser is only a diagnostic device, these steps can be skipped without affecting the fabrication of the photonic crystal laser as long as electon-beam lithography is used to pattern the sub-micron features. However, many of the processes that are used in fabricating the photonic crystal laser also occur in steps 7-10. Hence, not only will the stripe laser help verify the quality of the III-V material; its fabrication will also serve as an initial test of the forthcoming fabrication processes.

The SiO_2 is typically used as a hard mask for the plasma etching of both phosphide and arsenide-based semiconductors. SiO_2 is first deposited using plasma-enhanced chemical vapor deposition (PECVD) and the wafers are then coated with positive photoresist. The photoresist is patterned, and the SiO_2 is then etched using reactive ion etching.

Indium containing material such as InP is typically etched with a combination of methane and hydrogen (CH_4/H_2), while GaAs is typically etched in a chlorine-based plasma such as a BCl_3 plasma. At the time of this work, hydrogen/methane etches were no longer available in NSL due to cross-contamination issues with other etches; a new dedicated hydrogen/methane etcher was being constructed elsewhere in the laboratory. A hydrogen/methane etch is available in the TRL PlasmaQuest etcher, but previous work [43] has shown that polymer formation during hydrogen/methane etching causes significant problems with subsequent etches. Specifically, a polymer coats the chamber and sample acting as an etch mask during subsequent etches. To remove the polymer a

series of chamber cleans and sacrificial etches must be performed. Cleaning the PlasmaQuest etcher requires a TRL staff person to disassemble and mechanically clean the chamber. One can also try different InP etch chemistries as in [53]. The use of a heavy, inert atom such as argon during the GaAs etch has been found to produce mirror smooth sidewalls [54].

Since photoresist can not withstand neither a BCl_3 etch or a hydrogen/methane etch, SiO_2 is used as a hard mask. To pattern the SiO_2, either photoresist or a metal such as nickel can be used as an etch mask. Initial work, using AZ5214 as a positive resist, showed that CF_4 should be used to dry etch the SiO_2, rather than the more common CF_4/O_2 combination, as the reactive O_2 in the plasma etches the photoresist. A two minute, 120°C hot plate post-bake of the AZ5214 photoresist also improved the ability of the photoresist to withstand the dry etching process. References [55-56] showed that a flood exposure of the resist, an optimized post-bake, a low DC bias, and a thin layer of SiN_x helped to obtain SiO_2 sidewall variations to less than 500Å. The use of SF_6 was also recommended over CF_4 for the etch chemistry. Since 500Å variations were observed for wet-etching arsenide-based semiconductor material (section 4.2.3), these methods should yield etch roughness comparable to wet-etching, but with vertical sidewalls.

4.3.2. **Steps 11-12: Electron-beam lithography or Focused Ion Beam etching for photonic crystal active region**

Two options, Focused Ion Beam etching (FIB), or electron beam lithography and subsequent etching are capable of patterning of the submicron features required for the active region of the microcavity laser. Focused ion beam etching requires no hard mask,

because features are directly written and etched with an ion beam making FIB an ideal choice. Initial contacts were made with Mr. Richard San Martin of FIB-X Corporation.

In electron-beam lithography, features are written into photoresist, implying that a hard mask such as SiO_2 is required and ensuing dry etches must be utilized. Specialized resists are required for the high resolution electron beam lithography process. Previous work [43] showed that hydrogen silsesquioxane (HSQ) can be used as a resist but can not be used as a hard mask, although the use of a thin layer of SiO_2 might alleviate the problems with HSQ. If HSQ is not used, a multi-step process using Poly(methyl methacrylate) (PMMA) resist has already been designed [43]. The top view of the process steps leading up to etching of the submicron features is shown in Figure 28.

At this point in the process either pieces of the wafer or full wafers can be fabricated. The mask set was designed with fairly stringent tolerances on all alignments. To guarantee operation, the masks can not be misaligned by more than 0.5μm during each exposure step.

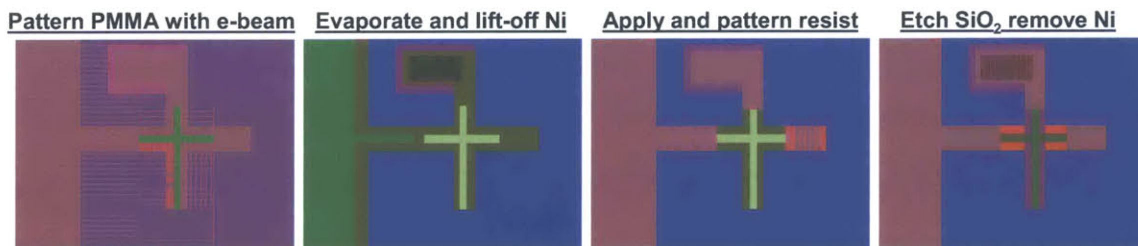

Figure 28: Electron-beam lithography process leading up to the etching of the submicron features. Some layer colors are made partially transparent to reflect actual visibility.

4.3.3. Steps 13-14: Undercut removal of Phosphide-based material

Undercutting, or the sacrificial etching of AlGaAs was thoroughly studied previously [50], in which GaAs features as long as 15μm were suspended in air. Since the

phosphide-based material is the material to be etched in this work, a different wet etch chemistry such as H_3PO_4:HCl (3:1) [49] will be required.

4.3.4. Step 15: Etching of SiO_2 to open up contact vias

The SiO_2 above the metal contacts is removed using negative photoresist as an etch mask. Although the complete removal of SiO_2 will enhance the index contrast of the entire structure, the SiO_2 etching process might cause etching damage to the active area or to the output waveguide. Therefore, SiO_2 is only removed from the metal contact pads to allow contact with a current probe.

4.3.5. Step 16: Thermal oxidation of AlAs

The oxidation process is critical to the photonic crystal laser design. Without the oxidation process, a parasitic *p-n* junction via the substrate exists in parallel to the microcavity lasers. Also, the output waveguide would rest atop a relatively high index cladding causing light to couple to the substrate. To ensure electrical isolation between the contacts, the width of the *p*-type contact pads are less than 110μm, allowing the AlAs underneath the pads to be fully oxidized while still allowing the pads to be sufficiently large for easy alignment to a current probe. Large scale oxidation of AlAs has been successfully demonstrated and studied by numerous researchers in the Integrated Photonic Materials and Devices Group.

4.4. Fabrication of a generic ridge laser

In order to test the quality of MBE-grown material, ridge lasers were fabricated with similar materials to those of the photonic crystal laser. Unlike the diagnostic stripe laser device described in Chapter 3, the ridge lasers were fabricated on different samples

than the photonic crystal laser. The ridge lasers also differ in how current is injected into the device. In the ridge lasers, current is injected from above through a top-side metal contact and from below, through bottom-side metal contact. Thus, current flows through the substrate and the lower AlAs layer. Consequently, the AlAs layer must be doped and cannot be oxidized, so that a low-resistivity current path exists from the bottom-side metal to the active region. A schematic of the ridge laser is shown in Figure 29 along with a fabrication sequence.

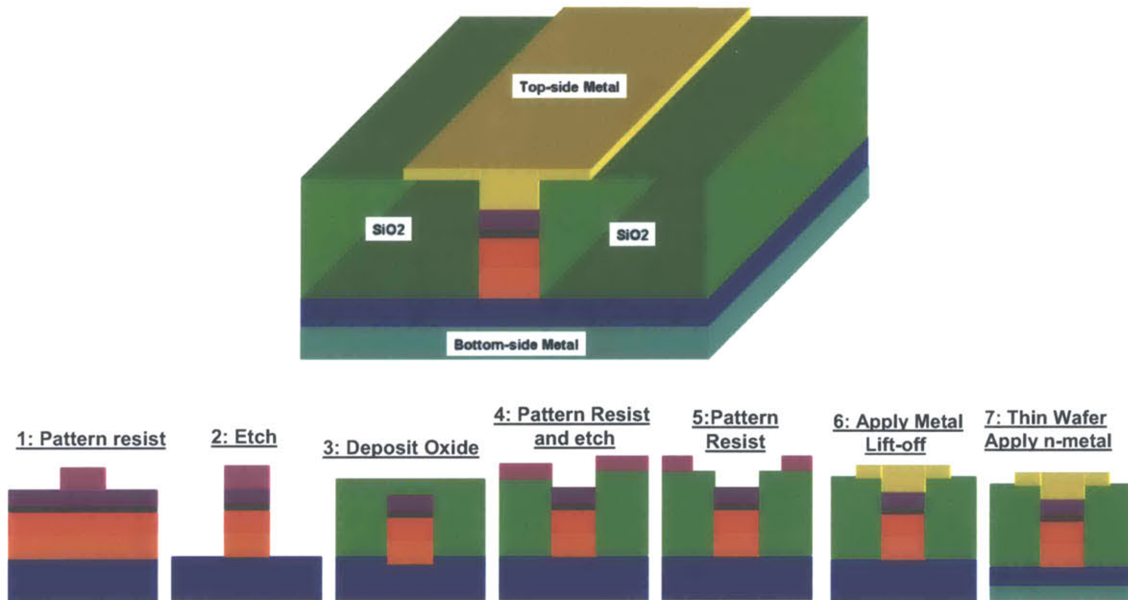

Figure 29: The ridge laser with accompanying fabrication sequence.

A process flow, employing self-aligned ohmic contacts, was also utilized, but the same metal-liftoff problems were observed. Also, the self-aligned contacts completely peeled off during the PECVD SiO_2 deposition.

Two sets of test wafers were grown specifically for the ridge laser. Sample VA36 was exactly like the quantum well sample, VA34, except that the lower AlAs layer was doped so that a bottom-side contact can be used. Sample VA37 was an experimental wafer containing 4 DWELL active regions and a digital alloy for the output waveguide.

The quantum dot wafer, sample VA37, emits at 1250nm but its emission width is quite broad in comparison to the photoluminescence from the strained quantum well wafer, sample VA36 as shown in Figure 30.

VA36
10nm GaAs: Be
125nm $Al_{.49}Ga_{.51}As$: Be
15nm GaAs
8nm $In_{.15}Ga_{.85}As$
15nm GaAs
8nm $In_{.15}Ga_{.85}As$
15nm GaAs
25nm $Al_{.49}Ga_{.51}As$
400nm n-$In_{.53}Ga_{.47}P$: Si
500nm AlAs: Si
GaAs: Si Buffer
GaAs Substrate

VA37	
10nm p-GaAs: Be	
125nm p-$Al_{.49}Ga_{.51}As$: Be	
35nm GaAs	
5nm GaAs	X4
6nm $In_{.15}Ga_{.85}As$	X4
.85nm InAs	X4
2nm $In_{.15}Ga_{.85}As$	X4
10nm GaAs HighT	X4
5nm p-GaAs:Be HighT	X4
20nm GaAs HighT	X4
5nm GaAs	
25nm $Al_{.49}Ga_{.51}As$	
19nm n-$In_{.53}Ga_{.47}P$: Si	
1nm n-GaAs: Si	X19
19nm n-$In_{.53}Ga_{.47}P$: Si	X19
500nm n-AlAs: Si	
GaAs: Si Buffer	

Grown Structure PL

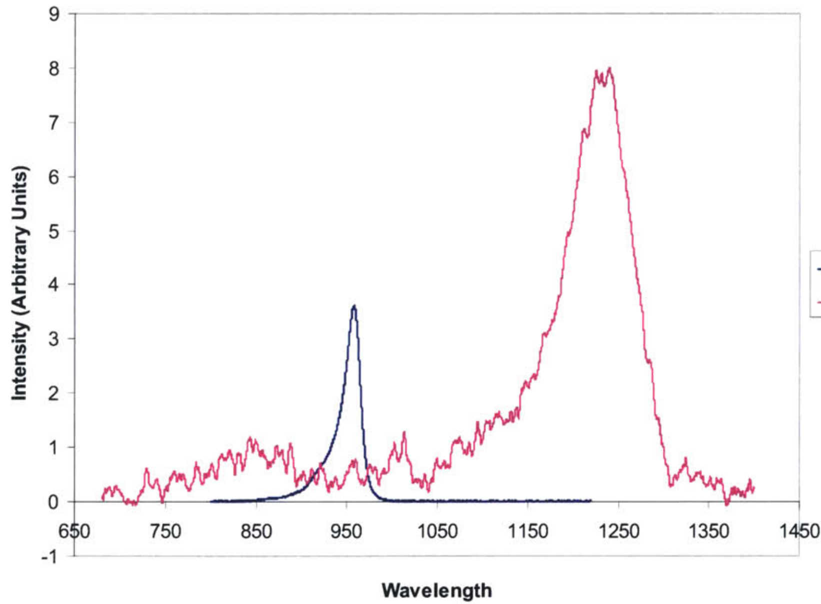

Figure 30: Grown structures and measured PL data.

The photonic crystal lasers and generic ridge lasers were fabricated in parallel up to process step number 6 of the photonic crystal laser process flow. Unfortunately, the metal adhesion problems were not discovered until both sets of wafers were processed. Thus, the only wafer that went through the desired process flow was sample VA36 wafer number two. Due to damage to the lapping equipment, the wafers could not be lapped, thus a final step still remains to be completed before the lasers can be tested. Figure 31 shows sample VA36 before the top metal was evaporated.

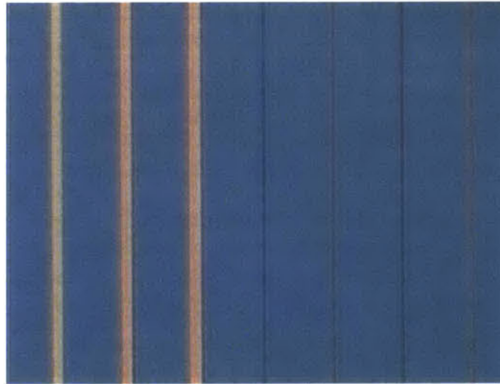

Figure 31: Sample VA36 before the second contact deposition. Stripes widths are as small as 1.5μm

As a comparison to the photonic crystal microcavity laser, the same rate equation analysis was employed to predict the L-I curves for the ridge laser. As shown in Figure 32, the sharp transition in the emitted power at threshold, which does not occur for microcavity lasers, does occur for the ridge lasers. As previously mentioned, microcavity lasers generate a large proportion of photons into the lasing mode before the onset of stimulated emission, thus the microcavity photonic crystal appears thresholdless on an L-I curve.

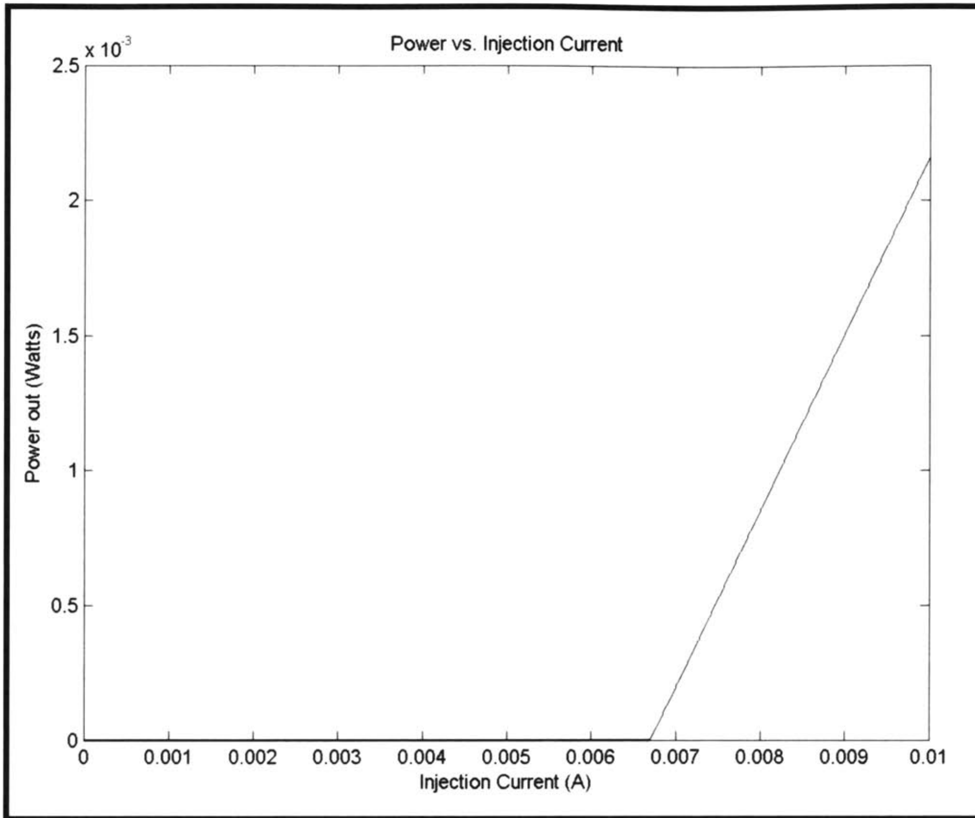

Figure 32: L-I curves for a ridge laser

Chapter 5.

Conclusion and Future Research

5.1. Further Investigations

5.1.1. Improvement to the rate equations

The rate equation analysis presented in Chapter 3, and elaborated on in Appendix 2, contained many assumptions. In particular, the proportion of photons exiting the output mirror was assumed to be ½ meaning the two mirrors of the Fabry-Perot laser cavity were assumed to have equal reflectivity. This assumption simplified the rate equations by avoiding the details of how the light intensity as a function of space varies with the reflectivity of the mirrors. A more accurate model utilizing the laser rate equations is found by decomposing the resonant mode into counter-propagating waves [57]. The probability distribution of the photon density for each wave can be found from [32],

$$\frac{d N_p{}^{\pm}}{d z} = \Gamma g N_p{}^{\pm} + \frac{1}{2}\frac{V}{V_p}\beta_{sp} B N^2 - <\alpha> N_p{}^{\pm} \tag{10}$$

where $N_p^{\pm}$ is the photon density traveling in either the plus, or minus, z-direction. The ½ factor in front of the lasing mode spontaneous emission rate accounts for the equal chance of photons being spontaneously emitted into each of the counter-propagating waves. The above equation can be solved using a finite-difference technique already developed for Semiconductor Optical Amplifiers [30], in combination with the carrier density equation already introduced in Chapter 3. The boundary conditions at the mirrors

(figure 33) can then be applied to determine both the solution to $N_p(z)$, and the output power.

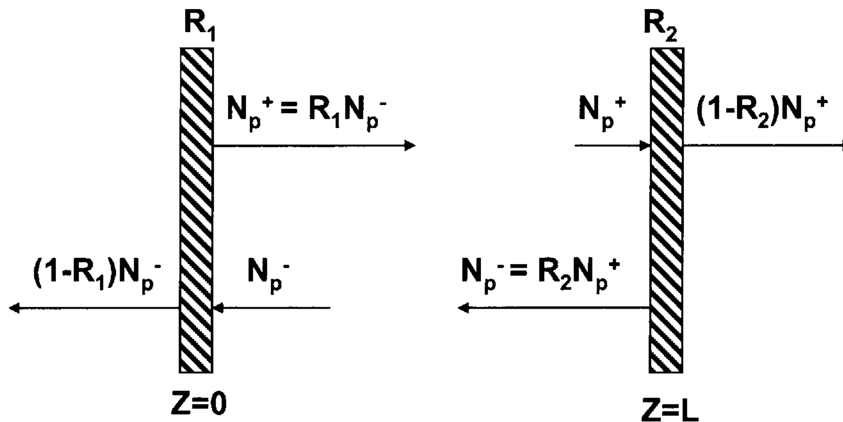

Figure 33: Boundary conditions for an optical cavity.

5.1.2. Testing of the Photonic Crystal Microcavity Laser

In Chapter 3, the output power of the microcavity laser was predicted to be on the order of microwatts. A small output power, in conjunction with coupling and propagation losses associated with the output waveguide, will make it difficult to detect the output light. One way to confirm the successful lasing of the device is to observe light exiting the top of the laser. Light exiting the top of the laser does not fulfill the total internal reflection condition because it was either scattered or is the result of spontaneous emission into a non-resonant mode. Thus, one would observe a noisy output from the top of the laser. However, once threshold is reached, a majority of the light in the cavity is the result of stimulated emission into the lasing mode. Undoubtedly some of the lasing mode photons will scatter and exit the laser vertically, so one can still observe line-width narrowing from this vertical output. In fact, many of the lasers presented in Chapter 2 were the result of light exiting the cavity vertically through so-called leaky modes. To ensure enough light leaks out of the top, one must pattern extra holes in the bottom

waveguide to increase the reflectivity of the photonic crystal mirrors. This method will confirm successful lasing, while eliminating the complication of coupling and propagation losses.

5.1.3. A laser incorporating adiabatic tapers

Because the gain medium resides above the output waveguide, there is a trade-off between the modal gain and the laser output power. To minimize this tradeoff, an alternative design[5] is proposed and is shown in Figure 34. The design employs adiabatic tapers to gradually vary the effective index as light approaches the output waveguide from the cavity. By gradually removing material from the top surface, the optical mode couples into the bottom waveguide with a minimum of loss. This design does require a different mask set along with greater fabrication precision to form the tapers. Therefore, it should only be attempted after the original laser design is successfully demonstrated.

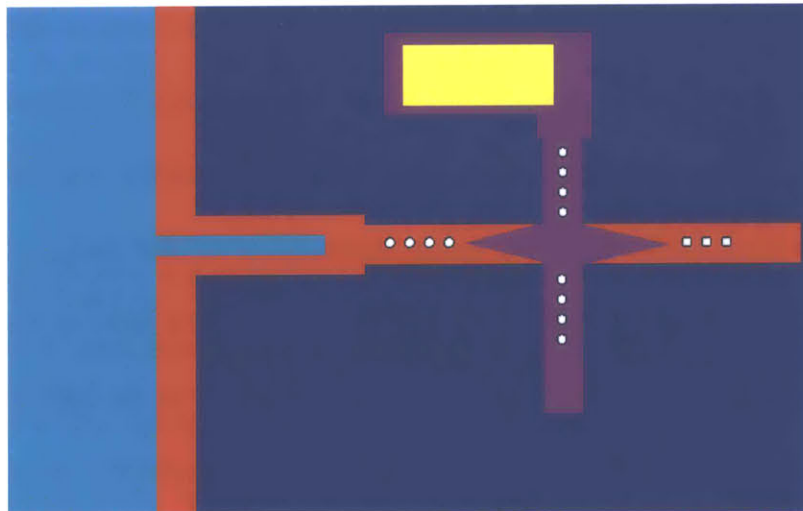

Figure 34: Top view of a photonic crystal laser utilizing adiabatic tapers

5.1.4. A microcavity laser with mirror confinement in three directions

The modes of an optical resonator can be broadly separated into three categories.

[5] The alternative design was suggested by Dr. Gale Petrich

1.) Modes, which satisfy the boundary conditions of a resonator and are totally internally reflected at all interfaces, are referred to as resonant modes. The lasing mode of a resonator is classified as a resonant mode.

2.) Modes, which do not satisfy the boundary conditions of their environment and can not exist, are called evanescent. These modes carry no time average power [58], and hence, by conservation of energy, an atom can not emit a photon into one of these modes. The effect of a cavity is to add more restrictions on the boundary conditions, so that more modes are evanescent.

3). Modes, which satisfy all the boundary conditions of the resonator yet are not totally internally reflected at one or some of the interfaces, are commonly referred to as leaky or radiation modes. Reflectors such as photonic crystals or gold mirrors can be used to reflect light of certain frequencies forcing the light to be totally internally reflected and thus eliminate many of the radiation modes. In eliminating radiation modes, these reflectors eliminate vacuum modes which can induce a medium to spontaneously emit photons into these lossy modes. It would thus be advantageous to create a microcavity laser confined by perfect mirrors in all directions, so that radiation modes can be suppressed.

One example of such a microcavity is the spherical Bragg resonator, a "Bragg onion resonator" [59], but it is unclear how a gain medium can be incorporated into the structure. A new laser structure that is capable of trapping light with mirrors in almost all directions is proposed and is schematically shown in Figure 35. Both of the proposed structures utilize a two-dimensional photonic crystal slab to confine light laterally. The light is coupled into a photonic crystal waveguide and exits the laser in the plane of the chip. Both proposed structures also utilize Bragg reflectors to confine light vertically and to isolate the light from the substrate. The Bragg reflectors can be partially oxidized similar to an oxide confined vertical cavity surface emitting laser (VCSEL), so that a higher index contrast exists in the photonic crystal slab. The lateral oxidation front must be precisely controlled in order to construct a conductive path from the bottom-side contact to the active region. The structure in Figure 35a. incorporates Bragg gratings vertically around the active region to confine the light in the vertical direction. In Figure

35b, a conducting low index dielectric, indium tin oxide (ITO) is placed above the active region. The ITO confines light by index confinement, and the top-contact also acts as a mirror to reflect any light which propagates vertically through the ITO. The incorporation of ITO allows for a layered structure that would be simpler to integrate with other optical components.

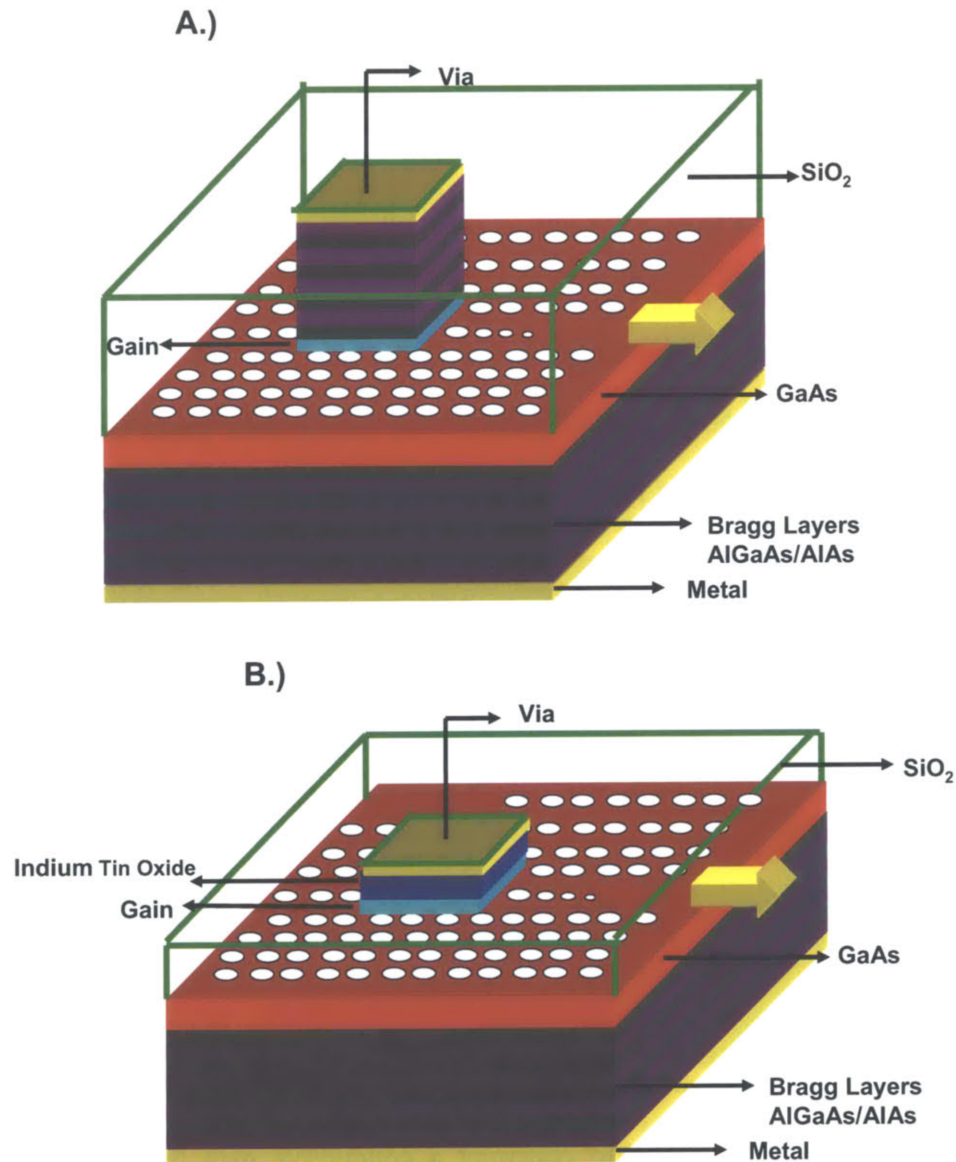

Figure 35: 2 variations of a 3D mirror confined microcavity laser

Each of these lasers provide quasi three-dimensional confinement meaning that spontaneously emitted light is less likely to couple into radiation modes. Mirror confinement is desired over index-guided structures, because index-guided structures allow a near continuum of vacuum modes to be present in the laser oscillator. This is due to the nature of index confinement, which operates on the principle that light approaching an interface at an angle greater than the critical angle will not be totally internally reflected. Thus, there is a finite cone of modes in k-space which are not totally internally reflected (sometimes referred to as an extraction cone), and can thus be characterized as radiation modes. Consequently, mirror-guided structures will drastically increase the spontaneous emission factor. Additionally, the proposed laser is edge emitting and is electrically activated making such a laser suitable choice for integrated optics.

5.2. Final Conclusions

The field of microcavity research is now widespread, and microcavities are just beginning to find permanent applications. A microcavity laser has recently been applied to the field of biomedicine, where it is used to detect tumor cells during surgery [60]. When combined with special filters, the refractive index change in microcavities can also be used to detect various chemical agents. Low-loss microcavities operating in the strong coupling regime are a viable source for quantum computation. Microcavity lasers have been theoretically and experimentally proven to outperform larger lasers in all categories with the exception of high output power. However, the lack of an electrically-activated, edge–emitting, microcavity laser has made it difficult for microcavity lasers to penetrate the field of integrated optics.

This thesis has presented the physics, design, and initial fabrication of a microcavity laser that is an excellent candidate as a light source for use in integrated optics. Using the phenomenon of vacuum fields, cavity quantum electrodynamics has been explained to provide a physical picture of spontaneous emission in a microcavity. A hybrid fabrication approach has been presented that should simplify the device processing. Problems with metal adhesion to *p*-type GaAs were encountered during fabrication, and various solutions to these problems have been suggested. The remaining fabrication steps have all been performed within the Integrated Photonic Materials and Device group. Suggestions from past members have been compiled to aid one in the remaining processing steps. The optical masks have been designed to ease testing, so that one can quickly qualify the optimal variation of the laser. When completed, the photonic crystal microcavity laser will represent a major improvement in edge emitting lasers. Finally, new microcavity lasers have also been proposed that could also find a niche in the field of integrated optics.

Appendix 1: Index of refraction for Al_xGaAs_{1-x}

```
%*Function calculates the refractive index of Al_xGa_1-x. User inputs x and
%the wavelength in meters
%All formulas and functions taken from Chuang "Physics of Optoelectronics
%Devices, 1995. pp. 249.
h=6.63e-34; %Planks constant
h_bar=h/(2*pi);
c=3e+8; %speed of light
c_cm=3e10;  %Speed of light in centimeters.
h_cm=4.14e-15;  %Plank constant in microelectronic untis.
hbar_cm=h_cm/(2*pi);

kt=.0259;  %Thermal voltage in eV

epsilon0=8.85e-12;  %Value in meters
epsilonGaAs=13*epsilon0;   %The permittivity of GaAs
q=1.6e-19;  %Charge of electron

%******************************************************************************
lambda=1.3e-6; %INPUT WAVELENGTH IN METERS
%*****************************************************************************
w=c*2*pi/lambda;
Ep=h*c/(q*lambda);  %Photon energy in eV
%******************************************************************************
x=.48;  %INPUT PROPORTION OF ALUMINUM
%******************************************************************************
Eg=1.424+1.266*x+.26*(x)^2; %Bandgap of AlGaAs in eV
delta=.34-.5*x;
A=6.64+16.92*x;
B=9.2-9.22*x;
yso=Ep/(Eg+delta);
y=Ep/Eg;
fy=1/y^2*(2-(1+y)^.5-(1-y)^.5);
fyso=1/yso^2*(2-(1+yso)^.5-(1-yso)^.5);

EpsilonFactor=(A*(fy+.5*(Eg/(Eg+delta))^(1.5)*fyso))+B;

n_AlGaAs=EpsilonFactor^.5
```

Appendix 2: The Phenomenological Rate Equations

The carrier rate equation can be written as,

$$\frac{dN}{dt} = \eta_i \frac{I}{qV} - CN^3 - BN^2 - A_d N - A_{surf} N - v_g \frac{V_p}{V} \Gamma g N_p$$

Equation A 1

where N is the free carrier density in the active region (cm^{-3}), and N_p is the lasing mode photon density in the laser cavity (cm^{-3}).

- $\eta_i \frac{I}{qV}$ is the generation rate of carriers in the active region due to pumping. Thermal generation of carriers does not have to be accounted for, because it is cancelled by the thermal equilibrium recombination rate. I is the terminal current (Amps), while V is the volume of the active material (cm^3). η_i is the injection efficiency - the fraction of carriers actually injected into the active medium. Carriers can be lost before reaching the active material through recombination, or they can leak out of the non-infinite quantum well after being injected.
- CN^3 is the carrier loss rate due to Auger recombination. Since Auger recombination requires three carriers, the rate is proportional to N^3 for intrinsic active materials. C is the Auger recombination coefficient (cm^6/s).
- BN^2 is the loss rate of carriers through spontaneous emission into all modes, R_{sp}. Since spontaneous emission requires a free electron and a free hole, the recombination rate is proportional to the NP product, but charge neutrality in the undoped active material demands $N=P$. The square law actually only holds in the Boltzmann limit, but it is very common to assume that it holds for larger carrier densities. The factor B is the biomolecular recombination coefficient (cm^3/s). In reality, this factor is affected by the cavity surrounding the gain medium and is not a strict material parameter. However, the net recombination rate is assumed to be a material parameter in this thesis, with only the coupling to the lasing mode being affected by the cavity.
- $A_d N$ is the carrier loss rate due to defects. In this thesis, high quality active material is assumed so that A_d can be set to zero.
- $A_{surf} N$ is the carrier loss rate due to surface recombination in the active region. The surface recombination coefficient, A_{surf}, is given by, $A_{surf}=v_s a_s/V$ where a_s is the exposed surface area of the active region (cm^2) and v_s is the surface recombination velocity (cm/s). The term $v_s N$ is simply the flux of carriers at the surface and a_s/V simply spreads out the flux over the gain region. The surface recombination velocity is much larger for exposed surfaces than for the surfaces between epilayers, so the surface area is given by a_s=2T(L+W) where T,L and W are thickness, length and width of the active material respectively.
- The term, $v_g \frac{V_p}{V} \Gamma g N_p$ is the stimulated emission rate into the lasing mode. It is noted that stimulated emission can occur into other modes, but high spectral purity is naturally assumed in this laser so that stimulated emission into the

lasing mode is dominant. The gain, g (cm^{-1}) is empirically modeled as, $g=g_o\ln(N/N_{tr})$ where g_o is the large signal gain and N_{tr} is the transparency carrier density. Γ is the confinement factor which in most practical cases is simply the photon energy in the gain region divided by the photon energy in the entire cavity for the lasing mode. Often, Γg is referred to as the modal gain. The term, V_p/V where V_p is the cavity volume (cm^3), is a weighting factor accounting for the difference in volume between the gain region and optical cavity. Finally, since material gain is defined in terms of length, multiplication by the group velocity, v_g (cm/s) converts the gain to a per unit time basis. The group velocity is given as c/n_{eff} where n_{eff} is the effective index which was calculated from the *Optiwave* simulations.

The photon rate equation is written,

$$\frac{dN_p}{dt} = v_g \Gamma g N_p + \frac{V}{V_p}\beta_{sp} B N^2 - v_g < \alpha > N_p$$

Equation A 2

- The spontaneous emission rate into the lasing mode, R'_{sp} is given as, $\beta_{sp}BN^2$ where β_{sp} is the spontaneous emission factor, which can be understood as R'_{sp}/R_{sp}. Where $R_{sp}=BN^2$ is the net spontaneous emission rate. The confinement factor for the lasing mode, Γ, is actually buried in the spontaneous emission factor, as spontaneous emission into the lasing mode is impossible for $\Gamma=0$. The term, V/V_p in front of the spontaneous emission factor accounts for the difference in volume between the gain medium and optical cavity.
- $v_g<\alpha>N_p$ is the photon loss rate where $<\alpha>$ is the modal loss (cm^{-1}). The modal loss can be broken up into the external loss due to mirrors $<\alpha_m>$ and the modal loss due to internal loss processes, $<\alpha_i>$. By assuming a Fabry Perot cavity, the mirror loss is, $<\alpha_m>=\frac{1}{L}\ln(\frac{1}{\sqrt{R_1R_2}})$ where R_1 and R_2 are the power reflection coefficients of the two mirrors and L is the axial length of the cavity. This equation explicitly shows how shorter cavities experience a greater mirror loss rate. The photonic crystal reflectors can actually introduce a phase shift to the oscillating field [61] so in reality the effective length of the cavity must be altered to maintain real reflection coefficients [61]. However, this effect was ignored in the calculations. The internal modal loss can further be written as the loss due to free carrier absorption, scattering, and traps. Photon loss due to direct band absorption is accounted for in the material gain which is negative if the material is absorbing.

Setting Equation A1 equal to zero and solving for the photon density gives,

$$N_p = \frac{\frac{V}{V_p} \beta_{sp} B N^2}{v_g < \alpha > - v_g \Gamma g}$$ **Equation A 3**

One can then set the carrier rate equation equal to zero and substitute the above value for N_p into it. The resulting equation is,

$$0 = \eta_i \frac{I}{q V} - C N^3 - B N^2 - A_d N - A_{surf} N - \frac{v_g \Gamma g \beta_{sp} B N^2}{v_g < \alpha > - v_g \Gamma g}$$ **Equation A 4**

Thus, a single equation is obtained where the only unknowns are the injection current $\eta_i I$, and the carrier density, N. This equation is solved by plugging in a value for I, and then calculating the value of N that produces a result equal to zero. The function fzero in Matlab is used. Before threshold, the initial guess value for fzero is simply the previous value. After threshold, the guess is modified to be just smaller than the asymptotic value that N approaches. This is necessary because Matlab falsely interprets singularities as intercepts. To find this asymptotic value one simply sets the loss equal to the gain. Assuming a logarithmic gain model, the resulting equality is,

$$< \alpha > = \Gamma g_o \ln \left(\frac{N}{N_{tr}} \right)$$ **Equation A 5**

Solving for N in the equation above yields the asymptotic value that the carrier density approaches. It is noted that this method is slightly different than the more common method of simply assuming a logarithmic carrier density and plugging a pre-defined carrier density into the rate equations. In the method presented here, the carrier density as a function of current naturally results from the rate equations.

Input	Description	Value Used	Units
λ	wavelength of lasing light	9.60E+02	nm
L_z	Axial cavity length	0.6	μm
W	Horizontal Cavity Width	0.6	μm
t_p	Vertical cavity thickness	0.675	μm
t	Active material vertical Thickness	0.01	μm
twg	Output waveguide thickness	0.4	μm
neff	Effective Index of cavity mode	1.819	
R	Power Reflectivities	0.99	
C	Auger Recombination Coefficient	4.00E-29	cm^6/s
B	Biomolecular recomb coefficient	7.00E-11	cm^3/s
v_s	Surface recomb velocity	1.50E+05	cm/s
N_{tr}	Transparency carrier density	1.80E+18	cm^{-3}
g_o	Large signal gain	2.10E+03	cm^{-1}
α(GaAs)	total loss coefficient for GaAs	2.85E+01	dB
α(InGaP)	total loss coefficient for InGaP	8.00E+00	dB

Table 2: List of values used in rate equation program

Following is the Matlab code used to simulate the rate equations.

```
%****************************************************************
%Code simulates the rate equations
%****************************************************************
warning off MATLAB:fzero:UndeterminedSyntax

%***********************************************************
%Fundamental Constants used in the code
%************************************************************
h=6.63e-34; %Planks constant
h_bar=h/(2*pi);
c=3e+8; %speed of light
c_cm=3e+8*100;%speed of light in centimeters/s
h_cm=4.14e-15;  %Plank constant in microelectronic untis.
hbar_cm=h_cm/(2*pi);

%*********************************************************
%Global Variables declared for use in a seperate function
%********************************************************
global V;
global C_auger;
global B;
global A_surf;
global Vp;
global Gamma;
global vg;
global go;
```

```
global Ntr;
global Bsp;
global alpha;
global Gamma_m;
global alpham;

lambda=960e-9;        %Free space assumed Wavelength in m.
lambda_cm=lambda*100;  %Wavelength in cm
w=c*2*pi/lambda;       %angular frequency in rad/sec is independant of material for
semiconductors
f=c/lambda;           %frequency in hertz independant of material your are in.

Lz=.6e-4;             %Length of active material volume and cavity volume in cm.
W=.6e-4;              %width of active material volume and cavity volume
t=.01e-4;             %thickness of active material volume
tp=.675e-4;           %thickness of the photon cavity volume
twg=.4e-4;            %thickness of output wg and thus mirror height
neff=1.819;           %Effective Index found from Optiwave simulations.
R=.99;                %Power reflection coefficient of PC mirrors
C_auger=4e-29;        %Auger coefficient for InGaAs GaAs QWELLs
B=.7e-10;             %Biomolecular recombination coefficient for QWeLLs
vs=1.5e5;             %Surface recombination velocity in bulk InGaAs p.151 of C&C
as=2*t*(Lz+W);        %surface area of active material
V=t*Lz*W;             %volume of active material
Vp=tp*Lz*W;           %photon cavity volume
A_surf=as/V*vs;       %Surface recombination coefficient
vg=c_cm/neff;         %group velocity in cm/s
Ntr=1.8e+18;          %Transparency carrier density
go=2100;              %Large signal gain
alphadBFreeCarrier=4;  %Free carrier loss coefficient in N-InP in dB.
alphadBTrap=1;         %Trap loss coefficient for InP in dB
alphadBScattering=3;   %Loss coefficient in InP due to scattering in dB. Could be more
due to small width
alphadBInP=alphadBFreeCarrier+alphadBTrap+alphadBScattering   %Total internal loss
coefficient for InP in dB
alphadBFreeCarrierGaAs=22;  %Free carrier loss coefficient for GaAs
alphadBTrapGaAs=3.5;   %Loss in GaAs due to deep traps
alphadBScatteringdB=3;  %Scattering loss for GaAs
alphadBGaAs=alphadBFreeCarrierGaAs+alphadBTrapGaAs+alphadBScatteringdB
%Total loss coefficient for GaAs
alphadB=twg/tp*alphadBInP+(tp-twg)/tp*alphadBGaAs;  %Weighted average of loss in
each material system.
                                   %gives modal loss. In reality could use
                                   %confinement factor for
                                   %each matarial
alpha=10^(alphadB/20)  %Value of loss coefficient in cm^-1
```

```
Gamma=V/Vp;            %Confinement factor for evenly distributed photon density
Gamma_m=twg/tp;        %output mirror confinement factor
alpham=1/Lz*log(1/R);  %mirror loss coefficient

loss=vg*alpha+vg*Gamma_m*alpham;  %The loss per unit time felt by mode
N_asymptote=Ntr*exp(loss/(Gamma*vg*go));   %The asymptotic value that N
approaches is value when gain=loss

for SpontIndex=1:1:6,
  Bsp=(SpontIndex-1)*9e-3+.005;  %vary spontaneous emission factor from .005 to .05
with 6 data points
  Nguess=1e18;       %Initial Guess for the carrier density at the lowest current input. A
value between
              %1e16 and 1e19 always works. This usually needs to be
              %adjusted if parameters change though. Otherwise Matlab
              %gives an error.
  ThresholdFlag=0;   %Initialize flag for reaching threshold to off
  m=0;           %Factor just to keep track of injection current
  index=0;
  delta=1e-6;       %Keeps track of increments in current. This should be adjusted in
                     %different situations
  for m=1:1:1e3,
    index=index+1;
    I=m*delta;
    Nfind=fzero('Rate',Nguess,[],I);
    Np(index)=V/Vp*Bsp*B*Nfind^2/(vg*(alpha+Gamma_m*alpham-
Gamma*go*log(Nfind/Ntr)));

Rst(index)=Vp/V*Gamma*vg*go*log(Nfind/Ntr)*Gamma*Bsp*B*Nfind^2/(vg*(alpha+
Gamma_m*alpham-Gamma*go*log(Nfind/Ntr)));
                                            %Stimulated emission rate is plotted for fun.
    Rsp(index)=Vp/V*Gamma*B*Nfind^2;  %Spontaneous emission rate is plotted
    gain=Gamma*vg*go*log(Nfind/Ntr);  %Value of gain for the given input current
    netgain(index)=gain-loss;       %Net gain is plotted for fun.
    Pout=.5*vg*alpham*Np(index)*Vp*h*f; %Value for output power
    Yaxis(index)=Pout;
    Xaxis(index)=I;
    Yaxis2(index)=Nfind;
    if ThresholdFlag==0   %Only perform the following when haven't reached
                          %threshold yet
      Nguess=Nfind;     %If haven't reached threshold, make the guess in fzero
                          %adaptable by setting equal to current value
      if Np(index)*Vp>1  %If haven't reached threshold, When have a total of 1
                          %photon in cavity then have reached threshold.
        ThresholdCurrent=I  %Print the threshold current to screen
        N_threshold=Nfind  %Keep the current threshold carrier value
```

```
            ThresholdFlag=1;    %Let program know threshold has been reached
          end              %end checking to see if one total photon in cavity.
        else               %Case when ThresholdFlag=1, when already reached threshold.
          Nguess=N_asymptote-1e14; %if reached threshold set the guess in fzero equal to
                                   %the value N approached asymptotically
                           %Must do this because fzero chooses the wrong value causing
                           %gain>loss which is unphysical.
        end                %End checking to see if have reached threshold
      end                  %End for loop containig injection current
      hold on;             %Keep the current graph on the axis to overlay graphs
      switch SpontIndex
         case 1,
          loglog(Xaxis,Yaxis,'k')
         case 2,
          loglog(Xaxis,Yaxis,'k')
         case 3,
          loglog(Xaxis,Yaxis,'k')
         case 4,
          loglog(Xaxis,Yaxis,'k')
         case 5,
          loglog(Xaxis,Yaxis,'k')
         case 6,
          loglog(Xaxis,Yaxis,'k')
        end              %End switch statement for deciding on color of graph
end                      %End for loop for different spontaneous emission factors
hold off;                %Next graph will start anew.
xlabel('Injection Current (A)');
ylabel('Power out (Watts)');
title('Power vs. Injection Current');
figure                  %Start a seperate graph
plot(Xaxis,Yaxis2,'k')
title('Carriers vs. Injection Current');
figure
plot(Xaxis,Rst,'k')
title('stim. emission rates vs. current');
figure
plot(Xaxis,Rsp,'k')
title('spont. emission rates vs. current');
figure
plot(Xaxis,netgain,'k')
title('net gain vs. current');

unction SteadyState=Rate(N,I)

global V;
global C_auger;
```

```
global B;
global A_surf;
global Vp;
global Gamma;
global vg;
global go;
global Ntr;
global Bsp;
global alpha;
global Gamma_m;
global alpham;
SteadyState=real(I/(1.6e-19*V)-C_auger*N^3-Vp/V*Gamma*B*N^2-A_surf*N-
    Vp/V*Gamma*vg*go*log(N/Ntr)*Gamma*Bsp*B*N^2/(vg*(alpha+Gamma_m*
    alpham-Gamma*go*log(N/Ntr))));
```

Bibliography

[1] D. Miller, *Dense optical Interconnections for silicon electronics,* in "Trends in Optics," Academic Press, New York (1992).

[2] D. Miller, *Optics for low-energy communication inside digital processors: quantum detectors, sources, and modulators as efficient impedance converters.* Optics Letters **14**, 146 (1989).

[3] J.D. Joannopoulos, R.D. Meade, and J.N. Winn, *Photonic Crystals*, Princeton, New York (1995).

[4] S.Y. Lin, *et al, A three-dimensional photonic crystal operating at infared wavelengths.* Nature **394**, 251 (1998).

[5] E. Yablonovich, *Photonic band-gap structures.* J. Opt. Soc. Am. B. **10**, 283 (1993).

[6] J.I. Pankove, *Optical Processes in Semiconductors,* Dover Publications, New York (1971).

[7] L.A. Coldren, S.W. Corzine, *Diode Lasers and Photonic Integrated Circuits.* John Wiley and Sons, New York (1995).

[8] B. Zhao, A. Yariv, Quantum Well Semiconductor Lasers, in *Semiconductor Lasers,* ed. E. Kapon, Ch. 1, Academic Press, San Diego (1999).

[9] H. Yokoyama, K. Nishi, T. Anan, Y. Nambu, S.D. Brorson, E.P. Ippen, M. Suzuki, *Controlling spontaneous emission and threshold-less laser oscillation with optical microcavities.* Optical and Quantum Electronics **24**, S245 (1992).

[10] Y. Yamamoto, S. Machida, G. Bjork, *Micro-cavity semiconductor lasers with controlled spontaneous emission.* Optical and Quantum Electronics **24** S215(1992).

[11] Y. Yamamoto, S. Machida, G. Bjork, *Microcavity semiconductor laser with enhanced spontaneous emission.* Physical Review A. **44**, 657 (1991).

[12] D.C. Kilper, P.A. Roos, J.L. Carlsten, K.L. Lear, *Squeezed light generated by a microcavity laser.* Physical Review A. **55**, R3323 (1997).

[13] R.J. Ram, "Microcavity Lasers: Coherent Matter and Light," Ph.D. Thesis, Electrical and Computer Engineering, University of California, Santa Barbara (1997).

[14] E.V. Goldstein, P. Meystre, Spontaneous Emission in Optical Cavities: A Tutorial Review, in *Spontaneous Emission and Laser Oscillation in Microcavities,* ed. H. Yokoyama, K. Ujihara, Ch. 1, CRC Press, Boca Raton, (1995).

[15] Peter W. Milloni, *The Quantum Vaccum.* Academic Press, INC. San Diego, CA, (1994).

[16] David J. Griffiths, *Introduction to electrodynamics.*Prentice Hall. Upper Saddle River, New Jersey, (1999).

[17] G. Bjork, S. Machida, Y. Yamamoto, K. Igeta, *Modification of spontaneous emission rate in planar dielectric microcavity structure.* Physical Review A. **44,** 669 (1991).

[18] J.M. Gerard, B. Sermage, B. Gayral, B. Legrand, E. Costard, V. Thiery-Mieg, *Enhanced spontaneous emission by quantum boxes in a monolithic microcavity,* Physical Review Letters. **81**, 1110 (1998).

[19] E.M. Purcell, *Spontaneous emission probabilities at radio frequencies*, Phys. Rev. **69**, 681 (1946).

[20] J.M. Gerard, B. Gayral, *InAs quantum dots: artificial atoms for solid-state cavity-quantum electrodynamics.* Physica E. **9**, 131 (2001).

[21] H. Benisty, J-M Gerard, R. Houdre, J. Rarity (eds.), *Confined photon systems*. Springer. Berlin, Heidelberg, (1999).

[22] G.M. Yang, M.H. Macdougal, P.D. Dapkus, *Ultralow threshold current vertical-cavity surface-emitting lasers obtained with selective-odidation.* Electronics Letters. **31**, 886 (1995).

[23] D.L. Huffaker, L.A. Graham, H. Deng, D.G. Deppe, *Sub-40μA Continuous-Wave Lasing in an Oxidized Vertial-Cavity Surface-Emitting Laser with Dielectric Mirrors*. IEEE Photonics Technology Letters. **8**, 974 (1996).

[24] H. Altug, D. Englund and J. Vuckovic, *Ultrafast photonic crystal nanocavity laser.* Nature Physics **2**, 484 (2006).

[25] H. Park, S. Kim, S. Kwon, Y. Ju, J. Yang, J. Baek, S. Kim, Y. Lee, *Electrically driven single-cell photonic crystal laser.* Science **305**, 1444 (2004).

[26] W.D. Zhou, J. Sabarinathan, P. Bhattacharya, B. Kochman, E.W. Berg, P. Yu, S.W. Pang, *Characteristics of a photonic bandgap single defect microcavity electroluminescent device.* IEEE J. Quant. Elec. **37**, 1153 (2001).

[27] T.D. Happ, M. Kamp, A. Forchel, J. Gentner, L. Goldstein, *Two-dimensional photonic crystal coupled-defect laser diode.* App. Phys. Lett. **82**, 4 (2003).

[28] R.J. Deri, E. Kapon, *Low-Loss III-V Semiconductor Optical Waveguides*. IEEE Journal of Quantum Electronics. **27**, 626 (1991).

[29] H.Y. Liu *et al. Improved performance of 1.3μm multilayer InAs quantum-dot lasers using a high-growth-temperature GaAs spacer layer.* Applied Physics Letters. **85**, 704 (2004).

[30] A. Markina, "Design and Simulation for the Fabrication of Integrated Semiconductor Optical Logic Gates," Ph.D. Thesis, Department of Electrical Engineering and Computer Science, MIT (2005).

[31] Ioffe-Physico-Technical Institute. (2003). *Physical Properties of Semiconductors. Retrieved Dec. 18, 2006 from New Semiconductor Material Archive:* http://www.ioffe.rssi.ru/SVA/NSM/Semicond/index.html

[32] S.L. Chuang, *Physics of Optoelectronic Devices,* John Wiley and Sons, New York (1995).

[33] Rajeev Ram, 6.731 Lecture Notes: Semiconductor Optoelectronics, Theory and Design (2006)

[34] G. Bjork, A. Karlsson, Y. Yamamoto, *Definition of a laser threshold*. Physical Review A. **50**, 1675 (1994).

[35] T. Baba, T. Hamano, F. Koyama, K. Iga, *Spontaneous emission factor of a microcavity DBR surface-emitting laser*. IEEE Journal of Quantum Electronics. **27** 1347 (1991).

[36] K. Petermann, *Calculated spontaneous emission factor for double-heterostructure injection lasers with gain-induced waveguiding. IEEE Journal of Quantum Electronics,* **15**, 566 (1979).

[37] J. Vuckovic, O. Painter, Y. Xu, A. Yariv, A. Scherer, *Finite-difference time-domain calculation of the spontaneous emission coupling factor in optical microcavities*. IEEE Journal of Quantum Electronics. **35**, 1168 (1999).

[38] R.J. Ram, D.I. Babic, R.A. York, J.E. Bowers, *Spontaneous emission in microcavities with distributed mirrors*. IEEE Journal of Quantum Electronics. **31**, 399 (1995).

[39] R.J. Ram, E. Goobar, M.G. Peters, L.A. Coldren, J.E. Bowers, *Spontaneous emission factor in post microcavity lasers*. IEEE Photonics Technology Letters. **8,** 599 (1996).

[40] A. A. Erchak, "Enhanced Performance of Optical Sources in III-V Materials Using Photonic Crystals," Ph.D. Thesis, Department of Materials Science and Engineering, MIT (2002).

[41] G. Bjork, Y. Yamamoto, *Analysis of semiconductor microcavity lasers using rate equations*. IEEE Journal of Quantum Electronics. **27**, 2386 (1991).

[42] G. Bjork, A. Karlsson, Y. Yamamoto, *Definition of a laser threshold.* Physical Review A. **50**, 1675 (1994).

[43] E. Mattson, "Design and Fabrication of an Electrically-Activated Photonic Crystal Nanocavity Laser," S.M. Thesis, Department of Electrical Engineering and Computer Science, MIT (2005).

[44] J.A. Del Alamo, 6.742 lecture notes: Microelectronic Devices, an Integrated Approach. (2005).

[45] T.C. Shen, G.B. Gao, H. Morkoc, *Recent developments in ohmic contacts for III-V compound semiconductors*. J. Vac. Sci. Technol. B. **10,** 2113 (1992).

[46] J. Thiery, H. Fawaz, A. Leroy, G. Salmer, *Extremely low resistance Au/Mn/Ni/Au ohmic contact to p-GaAs*. J. Vac. Sci. Technol. B. **13(5)**, 2130 (1995).

[47] J.K. Abrokwah, J.H. Huang, J. Baker, T. Polito, W. Ooms, *NiZnAl-Based p-Type Ohmic Contacts on AlGaAs/InGaAs Heterostructures.* IEEE Transactions on Electron Devices. **40**, 1185(1993).

[48] T. Sanada, O. Wada, *Ohmic Contacts to p-GaAs with Au/Zn/Au Structure.* Japanese Journal of Applied Physics. **18**, L491 (1980).

[49] A.R. Clawson, *Guide to references on III-V semiconductor chemical etching.* Materials Science and Engineering. **31**, 1 (2000).

[50] K-Y Lim, "Design and Fabrication of One-dimensional and Two-dimensional Photonic Bandgap Devices," Ph.D. Thesis, Department of Electrical Engineering and Computer Science, MIT (1999).

[51] J.A. del Alamo, T. Mizutani, *AuGeNi ohmic contacts to n-InP for FET applications.* Solid-state Electronics. **31**, 1635(1988).

[52] V.G. Weizer, N.S. Fatemi, *Simple, extremely low resistance contact to n-InP that does not exhibit metal-semiconductor intermixing during sintering*. Appl. Phys. Lett. **62**, 2731 (1993).

[53] R.J. Shul *et al.*, *New plasma chemistries for dry etching of InGaAlP alloys: BI3 and BBr3.* J. Vac. Sci. Technol. B **16**, 2690(1998).

[54] S. Agarwala *et al, High-density inductively coupled plasma etching of GaAs/AlGaAs in BCl3/Cl2/Ar: A study using a mixture design experiment.* J. Vac. Sci. Technol. B **16** 511 (1998).

[55] F. Ren, S.J. Pearton, J.R. Lothian, C.R. Abernathy, W.S. Hobson, *Reduction of sidewall roughness during dry etching of SiO2.* J. Vac. Sci. Technol. B. **10**, 2407 (1992).

[56] R. Lothian, F. Ren, S.J. Pearton, *Mask erosion during dry etching of deep features in III-V semiconductor structures*. Semicond. Sci. Technol. **7**, 1199 (1992).

[57] Discussion with Professor Leslie Kolodziejski

[58] J.A. Kong, *Electromagnetic Wave Theory,* EMW (2000).

[59] Y. Xu, W. Liang, A. Yariv, J.G. Fleming, S-Y Lin, *High quality-factor Bragg onion resonators with omnidirectional reflector cladding*. Optics Letters. **28**, 2144 (2003).

[60] P.L. Gourley, *Biocavity laser for high- speed cell and tumour biology,* J. Phys. D: Appl. Phys. **36**, R228 (2003).

[61] E. Istrate, E.H. Sargent, *Measurement of the phase shift upon reflection from photonic crystals.* Applied Physics Letters. **86,** 151112 (2005).